

Energy-efficient Electrochromic Smart Windows

by

Wu Zhang

A thesis submitted in partial fulfillment of the requirements for the degree of

Master of Science

in

Cross-Disciplinary

Department of Civil and Environmental Engineering

University of Alberta

© Wu Zhang, 2020

Abstract

Smart windows, having electrically-controlled transmission and zero-energy consumption when maintaining a colored or colorless state, increase the energy efficiency of buildings because they offer the potential to greatly reduce the energy cost of lighting, heating and cooling. Currently, the operation of traditional smart windows requires external voltages to trigger the coloration/bleaching processes, which makes traditional smart windows far from being a net-zero energy-consumption technology. The purpose of this work was to develop energy-efficient electrochromic smart windows, which are addressed by electrochromic supercapacitors and electrochromic batteries.

Herein, the first study involved electrodeposition of MoO_{2+x} thin films with oxygen deficiencies. The electrodeposited MoO_{2+x} electrode exhibits a super-capacitive performance of 89 mF cm^{-2} at 1 mA cm^{-2} . This enhanced super-capacitive performance makes these electrodeposited MoO_{2+x} films highly promising candidates as counter electrodes in a complementary electrochromic device (i.e. electrochromic supercapacitor). As such, in comparison to the single-active-layer electrochromic device, the introduction of MoO_{2+x} electrode accelerates redox reactions at the working electrode (WO_3). We show that the coloration potential of the complementary electrochromic device decreases to -0.5 V and the bleaching potential reaches as low as 0.5 V . This research provides a new and facile strategy to fabricate sub-stoichiometric molybdenum oxide nanofilms and reveals the functions of super-capacitive materials in a complementary electrochromic device.

The second study involved the synthesis of aqueous V_3O_7 nanoparticle inks, which offers the potential for fabricating large-scale thin films via low-cost solution-processed techniques. The fabricated V_3O_7 electrode can be utilized in a Zn- V_3O_7 electrochromic battery display system that exhibits an optical transmittance contrast of 21% at 632.8 nm and rapid switching times of 10.4/28.6 s (coloration at 0.2 V/bleaching at 1.6 V). Moreover, the Zn- V_3O_7 electrochromic battery display system eliminates the external voltage requirement for the coloration process and retrieves 15.2 mWh g⁻¹ (32.6 mWh m⁻²) energy consumed for the bleaching process. For a proof of concept, a prototype aqueous Zn- V_3O_7 electrochromic battery display is constructed by sandwiching a Zn anode between two V_3O_7 cathodes. The demonstrated electrochromic battery display possesses an open circuit potential (OCP) of 1.38 V, which enables the self-coloration behavior and energy retrieval functionality. We also show that the prototype display reversibly switches between the multi-colors (fully yellow, fully grayish-blue and half yellow-half grayish-blue maple leaves). This research presents a facile strategy to synthesize aqueous V_3O_7 inks, as well as a novel electrochromic battery display having energy retrieval functions, thus facilitating the development of energy-efficient electrochromic displays.

Preface

This thesis is focused on the energy-efficient electrochromic smart windows. The research presented in Chapter 3 and Chapter 4 along with their supporting information is my original work.

Chapter 3 of this thesis has been published as Zhang, W.; Li, H.; Firby, C. J.; Al-Hussein, M.; Elezzabi, A. Y., “Oxygen-Vacancy-Tunable Electrochemical Properties of Electrodeposited Molybdenum Oxide Films,” ACS Applied Materials&Interfaces, vol. 11, issue 22, 20378–20385.

Chapter 4 of this thesis is under review as Zhang, W.; Li, H.; Al-Hussein, M.; Elezzabi, A. Y., “Electrochromic Battery Displays with Energy Retrieval Functions Using Solution-Processable Vanadium Oxide Inks,” Advanced Optical Materials, vol. 8, issue 2, 1901224.

All authors designed the experiments. I analyzed the data and wrote the manuscript. All authors contributed to editing the manuscript. A.Y.E. and M.A.H. supervised the project.

Acknowledgment

I would like to express my gratitude to my supervisor, Professor Mohamed Al-Hussein, and to my co-supervisor, Professor Abdulhakem Elezzabi, for their valuable advice and lessons during my master's program. Their guidance over the past two and half years has benefited me greatly in different ways. I thank them for their support in financing and producing my research works. I also want to say thank you to Alberta Innovates, Natural Sciences and Engineering Research Council of Canada, and All Weather Windows Ltd. for their support.

I truly appreciate Dr. Haizeng Li for his generous instruction during my research. Dr. Haizeng Li has taught me a lot of valuable skills, which has had a significant impact on my knowledge. Many thanks to him for his guidance and I enjoyed working with him.

I would also like to express my sincere appreciation to my parents and my long-time friends Muxi, Joyce, Zhen, Ruifan, Jiafu, and Danzhu for their companionship and support. I want to also express my gratitude to my research team members: Amir Badkoobehhezaveh, Ryan Boehnke, Curtis Firby, Eric Hopmann, and Nir Katchinskiy for their advice and assistance. I would like to devote my thesis to all of you and thank you.

Table of Contents

1	Introduction	1
2	Background	4
2.1	Electrochromic Materials.....	4
2.2	Complementary Electrochromic Devices	8
2.3	Electrochromic Batteries	11
2.4	Methods of Electrochromic Films Preparation.....	12
2.5	Parameters of Electrochromism.....	15
2.6	Discussion.....	16
3	Oxygen Vacancy Tunable Electrochemical Properties of Electrodeposited Molybdenum Oxide Films	18
3.1	Introduction.....	18
3.2	Experimental Section.....	21
3.3	Results and Discussion	24
3.4	Summary	33
4	Electrochromic Battery Displays with Energy Retrieval Functions Using Solution-Processable Vanadium Oxide Inks.....	35
4.1	Introduction.....	35
4.2	Experimental Section.....	38
4.3	Results and Discussion	40

4.4	Summary	50
5	Conclusion and Future Outlook	51
5.1	Conclusion	51
5.2	Future Outlook.....	52
	Appendices	53
	Appendix A: Characterization of molybdenum oxide films	53
	Appendix B: Characterization of vanadium oxide nanoparticle films	60
	References	65

List of Tables

Table 2-1: Wavelength for colors in visible region.....	15
Table 5-1: Comparison of current state-of-the-art smart windows.	51
Table A-1: Atomic ratio of Mo in MoO_{2+x} , MoO_{3-y} , and MoO_3 films.....	55
Table B-1: Atomic ratio of V^{4+} and V^{5+} in the as-deposited, reduced and oxidized vanadium oxide films.	64

List of Figures

Figure 1: Electrochromic window design	2
Figure 2-1: Electrochromic oxides showing both cathodic and anodic coloration ...	5
Figure 2-2: Schematic illustration of the change of MoO_3 crystal structure during ions insertion-extraction process	6
Figure 2-3: Complementary electrochromic device	8
Figure 2-4: Schematic diagram of the NiO/WO_3 electrochromic device	10
Figure 2-5: Electrochromic battery	11
Figure 2-6: Schematic representation of the two types of cathodic electrodeposition processes: (a) electroplating and (b) electrophoretic deposition (EPD).....	12
Figure 2-7: Schematic representation of the immobilization of TiO_2 nanoparticles on the surface of cellulose fiber of paper	13
Figure 2-8: Spray coating of pale blue solution	14
Figure 3-1: Structure and component analysis of electrodeposited MoO_{2+x} films.....	25
Figure 3-2: Electrochemical measurements of electrodeposited MoO_{2+x} films.....	27
Figure 3-3: Electrochromic performance of single-active-layer ECDs and complementary ECDs	30
Figure 3-4: Structure, component and electrochemical measurements of MoO_{3-y} films.....	33
Figure 4-1: Structure and component analysis of V_3O_7 nanoparticles.....	41
Figure 4-2: Electrochromic and electrochemical performance of V_3O_7 films	45
Figure 4-3: X-ray photoelectron spectroscopy analysis of V_3O_7 films.....	47
Figure 4-4: Electrochromic performance of $\text{Zn-V}_3\text{O}_7$ electrochromic battery display with energy retrieval function.....	49
Figure A-1: Schematic of MoO_{2+x} films electrodeposited on ITO glass	54
Figure A-2: Electrochemical impedance spectroscopy of MoO_{2+x} electrode	56

Figure A-3: Electrochemical impedance spectroscopy of MoO_{3-y} electrode and bare ITO substrate	57
Figure A-4: Cycle performance of MoO_{2+x} nanofilms.....	58
Figure A-5: Structure, component and electrochemical measurements of MoO_3 nanofilms	59
Figure B-1: Cyclic voltammetry measurement of V_3O_7 electrodes in 1M LiCl electrolyte and 1M ZnSO_4 electrolyte.	61
Figure B-2: Coloration Efficiency of V_3O_7 nanoparticle films.	62
Figure B-3: Cycle performance of the V_3O_7 nanoparticle films	63

List of Abbreviations

BF	Bright-field
CE	Coloration efficiency
CV	Cyclic voltammetry
DF	Dark-field
DI	Deionized
ECD	Electrochromic device
EIS	Electrochemical impedance spectroscopy
EPD	Electrophoretic deposition
FE-SEM	Field emission scanning electron microscopy
FTO	Fluorine doped tin oxide
HER	Hydrogen evolution reaction
ITO	Indium tin oxide
LED	Light-emitting diode
LSV	Linear sweep voltammetry
OCP	Open circuit potential
PEI	Poly(ethyleneimine)
PVA	Polyvinyl alcohol
RTEE	Round-trip energy efficiency
TEM	Transmission electron microscope
TMO	Transition metal oxide
XPS	X-ray photoelectron spectroscopy
XRD	X-ray powder diffraction

List of Symbols

Symbol	Meaning	Units
F	Faraday constant	96485 C mol^{-1}
n	Number of electrons transferred	dimensionless
T	Transmittance	dimensionless
η	Coloration efficiency	$\text{cm}^2 \text{ C}^{-1}$
C_A	Capacitance	mF cm^{-2}
Δt	Discharging duration	s
ΔV	Potential window	V
A	Area	cm^2
R_s	Internal Resistance	Ω
D	Diffusion coefficient	$\text{cm}^2 \text{ s}^{-1}$
C	Concentration	mol cm^{-3}
v	Scan rate	V s^{-1}

Chapter 1

Introduction

Meeting increasing energy demands has become a severe challenge all around the world. Because of the limitations of non-renewable resources, improving the efficiency of energy utilization is an urgent problem. In 2014, there were approximately 482,000 buildings in Canada that consumed a total of 911.2 million gigajoules of energy;^[1] therefore, the potential building energy saving is significant.

Electrochromic film technology provides a new method to save energy because it controls the solar radiation and transmittance of visible light through building windows on demand.^[2] Electrochromic films can be deposited on the surface of conductive glass, such as indium tin oxide (ITO) or fluorine-doped tin oxide (FTO) glass. When a voltage is applied to electrochromic films, the photochemical properties of the materials are altered in a reversible fashion.^[3] Applying a different range of voltage or using different electrochromic film materials will result in changing the color and transmittance properties of the window. Furthermore, the transmittance of windows can be maintained if the voltage applied is turned off. Therefore, by controlling the voltage applied to the electrochromic film, windows can reduce the energy loss that is caused by the temperature difference between the indoor temperature and the outdoor temperature. Hence, the energy spent on cooling or heating the buildings will be reduced.

The operation of a typical smart window is shown in Figure 1.^[4] There are three states of a smart window: bright (Figure 1a), cool (Figure 1b) and dark (Figure 1c). In the bright state

Introduction

(Figure 1a), both visible and near-infrared radiation are transmitted through, and the transmittance of the smart window is close to that of traditional plain glass windows. After applying a voltage, the intercalation of solute ions triggers a coloration process (cool state) (Figure 1b), which blocks most of the near-infrared light. Upon applying a more voltage, both visible and near-infrared lights are blocked with the formation of a dark state (Figure 1c). These three states can be reversibly switched by controlling the voltage applied to smart windows.

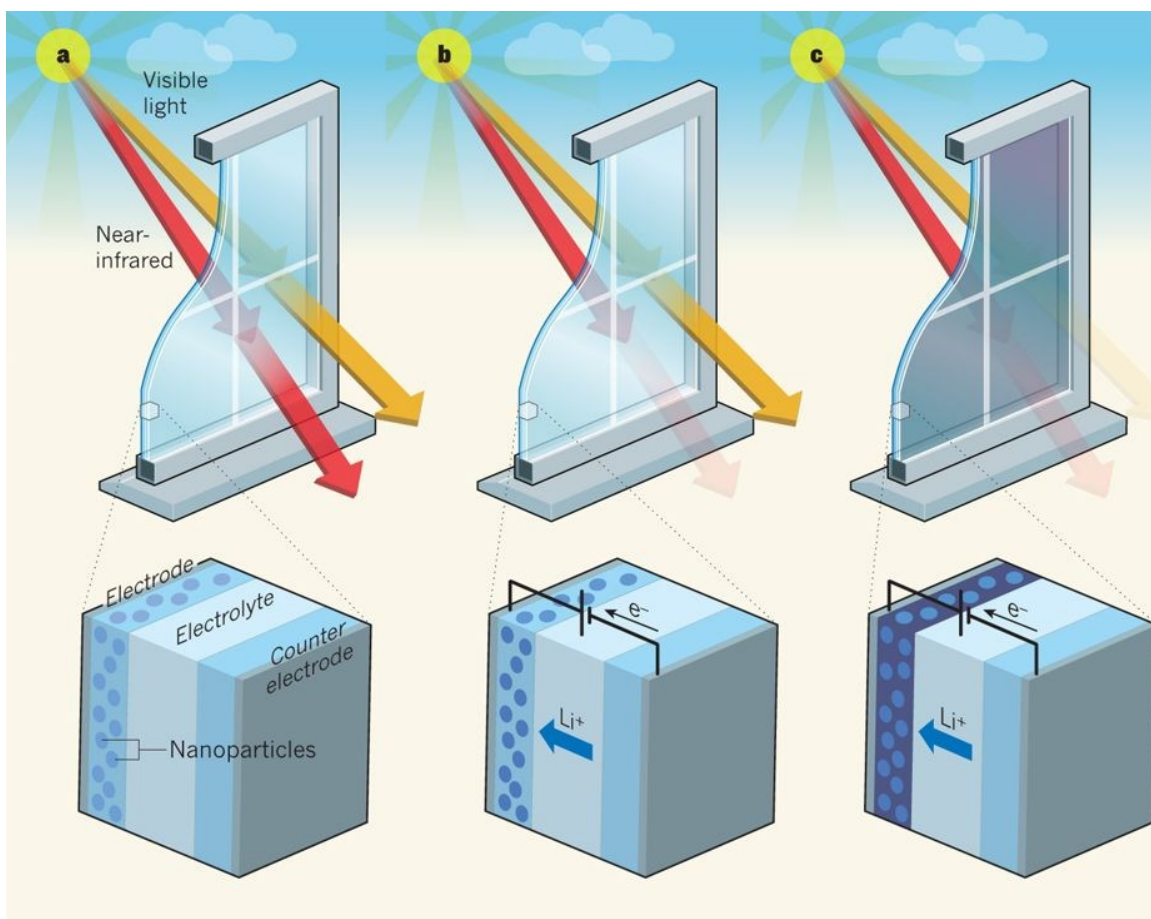


Figure 1. Electrochromic window design that controllably and selectively absorbs visible light and near-infrared light. Reprinted with permission from Ref. [4]. Copyright 2013, Nature Publishing Group.

The electrochromism Phenomenon was firstly introduced in 1961 by Dr. J. R. Platt from the University of Chicago.^[5] In 1969, Dr. S. K. Deb explained in detail the electrochromic performance of WO₃ films.^[6] Subsequently, researchers in the field of electrochromism discovered numerous electrochromic materials, including transition metal oxides and organic electrochromic materials. Recently, electrochromism technology has been applied to the development of smart windows. Compared to the smart window, a traditional window is responsible for the loss of approximately 30% of the energy loss during either cooling or heating a building.^[7] In this respect, windows can be considered ‘holes’ in building envelope and a significant portion of energy can escape through these holes. On the other hand, smart windows block 99.4% of ultraviolet light, which significantly reduces the energy losses of a building caused by a temperature differential. According to the United States (U.S.) Department of Energy, smart windows could save as much as 1 quadrillion BTUs of energy every year, which is more than 1 percent of the nation’s annual energy consumption, or more than \$10 billion in annual energy costs in the U.S.^[7] This is further proved by the study “The Energy-Savings Potential of Electrochromic Windows in the US Commercial Buildings Sector” from Lawrence Berkeley National Laboratory.^[8] Building simulations have been performed to evaluate the energy performance of smart windows in commercial buildings. Here, smart windows enable a reduction of 10-20% energy consumption compared to static low-emissivity windows. Thus, smart windows are a promising technology for energy-efficient green buildings

Chapter 2

Background

2.1 Electrochromic Materials

Electrochromic materials are the most important part of the electrochromic device. Normally, they can be divided into organic and inorganic materials. WO_3 is a widely used inorganic material due to its excellent electrochromic properties and high electrochemical stability.^[3] Conductive polymers are widely used organic material because of their various color selectivity, high conductivity, and fast reaction time.^[9]

2.1.1 Inorganic Materials

Transition metal oxides are a widely used inorganic material. According to the voltage of the colored state, they can be classified into cathodic coloration and anodic coloration^[10] materials as shown below in Figure 2-1:

ELECTROCHROMIC OXIDES:

H																	He
Li	Be											B	C	N	O	F	Ne
Na	Mg											Al	Si	P	S	Cl	Ar
K	Ca	Sc	Ti	V	Cr	Mn	Fe	Co	Ni	Cu	Zn	Ga	Ge	As	Se	Br	Kr
Rb	Sr	Y	Zr	Nb	Mo	Tc	Ru	Rh	Pd	Ag	Cd	In	Sn	Sb	Te	I	Xe
Cs	Ba	La	Hf	Ta	W	Re	Os	Ir	Pt	Au	Hg	Tl	Pb	Bi	Po	At	Rn
Fr	Ra	Ac															


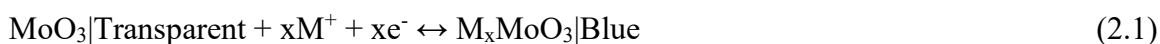

Cathodic coloration
Anodic coloration

Figure 2-1. Electrochromic oxides showing both cathodic and anodic coloration. Reprinted from Ref. [10]. Copyright 2017, Elsevier.

Cathodic Coloration

Cathodic coloration means that the electrochromic films are bleached by applying a positive voltage and color by applying a negative voltage. WO_3 , MoO_3 , TiO_2 , and Nb_2O_5 are widely used cathodic electrochromic materials. For example, the model of coloration of MoO_3 (Figure 2-2) is represented by the reaction shown in Equation 2.1:



M^+ is positive ions which can be either H^+ , or Li^+ , or Na^+ .

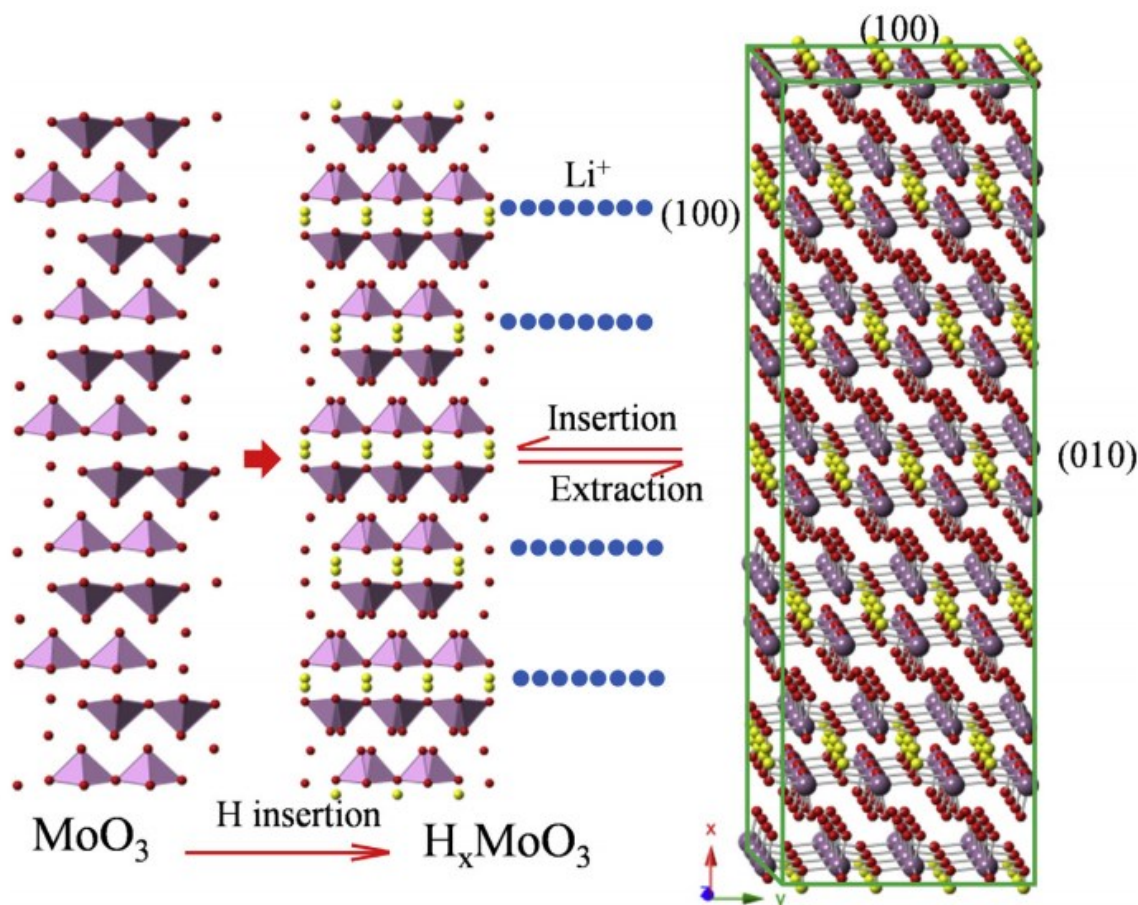
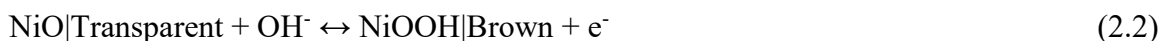


Figure 2-2. Schematic illustration of the change of MoO_3 crystal structure into H_xMoO_3 and the lithium-ion insertion-extraction process for H_xMoO_3 . Reprinted from Ref. [11]. Copyright 2015, Elsevier.

Ideally, MoO_3 is a composite of the octahedron. As shown in Figure 2-2, the two-layer structure of MoO_3 provides the possibility of ions insertion.^[11] The positive M^+ ions can be inserted into the gap between the two layers. However, since the Van der Waals' force between the two layers is week, this causes high coloration efficiency but low bleaching efficiency.

Anodic Coloration

Anodic coloration means that the electrochromic films are colored by applying a positive voltage and are bleached by applying negative voltage. NiO, IrO_x, and Co₂O₃ are widely used anodic electrochromic materials. For example, the model of the coloration of NiO can be explained by the reaction represented by Equation 2.2:



where, normally, KOH solution is used to be the source of OH⁻

NiO is the most widely used anodic electrochromic material due to the abundance in nature. This material has the same structure as NaCl,^[12] where both Ni²⁺ ions and O²⁻ ions are in the center of a regular octahedron. Moreover, because of the natural lack of Ni²⁺ ions in the structure, NiO is also behaving as a semiconductor.^[13]

2.1.2 Organic Materials

Organic materials are widely used because of their multi-colors, high electrochromic efficiency, and long-time stability. Conductive polymers and bipyridine-based compounds are often used in organic materials.^[14] Conductive polymers are a high molecular material with high conductivity. Electrons can move on the molecular chain, which provides the possibility of electrochromism. In recent research, polyaniline, polypyrrole, and polythiophene are often used conductive polymers.^[15] Viologen is the most often used bipyridine-based compound. Viologen has three redox states, which corresponds to multi-step electrochromism. Moreover, Viologen is colorful, stable, and heat-resist.^[14]

2.2 Complementary Electrochromic Devices

An electrochromic device is a “sandwich” structure that contains: substrate, transparent conductor, counter-electrode, ion conductor and electrochromic layer (the most important part) as shown below in Figure 2-3.

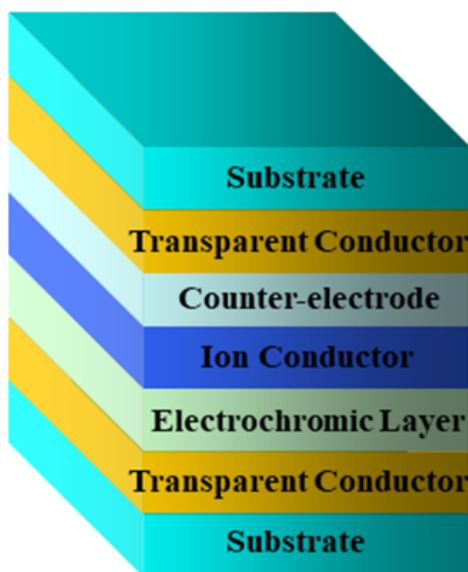


Figure 2-3. Complementary electrochromic device.

Substrate

The Substrate is the outer layer of the electrochromic device, which supports the device. It is typically made out of glass.

Transparent Conductor

The most important function of the transparent conductor is its ability to allow electrons flow. The transparent conductor can be either indium tin oxide (ITO) or fluorine-doped tin oxide (FTO). The composite of a substrate and transparent conductor is called ITO glass or FTO glass, respectively.

Counter Electrode

The counter-electrode is also known as the ions store layer. This electrode provides space for ion storage. When the voltage is applied to the electrochromic layer, electrons flow out of the electrochromic layer and enter the counter-electrode. Therefore, the counter-electrode must exhibit high ions storing capacity.

Electrochromic Layer

This is the most important part of an electrochromic device. It is also called the working electrode. The coloration and bleaching of electrochromic material occur in this layer.

Ion Conductor

The ion conductor layer (electrolyte) is used for the transport of ions. Based on the properties of the electrochromic layer, the electrolyte can be either an acid or an alkaline solution. Typically, the ion conductor is in a liquid state, which provides high efficiency in terms of ions transport. Some recent research studies showed that a solid ion conductor can also exhibit high working efficiency.^[16]

Example of NiO and WO₃ Complementary Electrochromic Device

The composite of NiO and WO₃ electrodes is an example of the complementary electrochromic device (Figure 2-4).^[17] Both NiO and WO₃ films can work as the electrochromic layer, which significantly increases the working efficiency. The opposing redox reactions occur at the electrodes in the complementary electrochromic device, while the WO₃ electrode is being oxidized (bleaching) or reduced (coloring), the NiO electrode

can be simultaneously reduced (bleaching) or oxidized (coloring) at the counter electrode. Hence, both NiO and WO₃ can be transformed to a colored state by applying a voltage. On the other hand, at the time that the opposite voltage is applied, both NiO and WO₃ layers can become transparent.

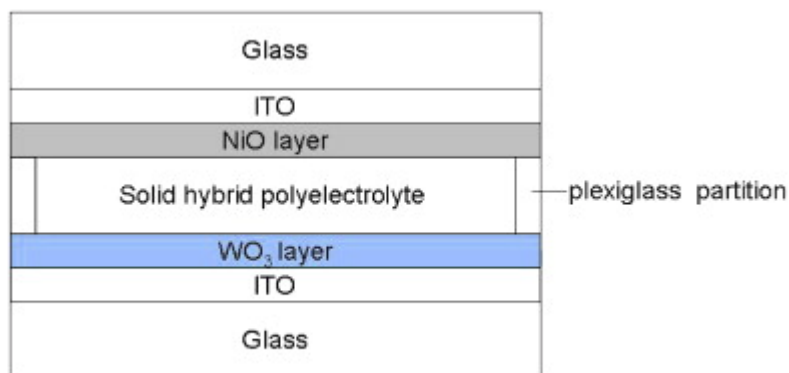


Figure 2-4. Schematic diagram of the NiO/WO₃ electrochromic device. Reprinted from Ref. [17]. Copyright 2009, Elsevier

Supercapacitive Materials

Supercapacitive materials are one example of promising energy storage materials. Such materials have been developed because of their desirable properties, such as large power density and high charge/discharge rate.^[18] Supercapacitive materials can also function as the ions store layer in a complementary electrochromic device. As the counter electrode, a supercapacitive material enhances the redox reaction at the electrochromic layer. Electric double-layer capacitor and pseudo-capacitor are two cores contributing to the high capacitance performance of supercapacitors.^[19] Supercapacitive properties have been found from various materials such as metal oxides, conducting polymers and binary metal hydroxides.^[20–22]

2.3 Electrochromic Batteries

Electrochromic materials change their colors in response to the intercalation of guest ions. Interestingly, the intercalation of the guest ions is very similar to the chemistry of batteries. In this regard, such material enables the functionalities of an electrochromic battery that incorporates energy storage and electrochromism features. When a versatile electrochromic material (cathode) embodies a higher potential compared to the anode (typically a metal), an electrical current can be generated by the conversion of chemical energy via redox reactions at the anode and cathode. Meanwhile, the intercalation of guest ions (redox reactions at the cathode side) induces the color change of the electrochromic materials. Such an electrochromic battery provides novel advantages compared to conventional electrochromic devices, including the elimination of the requirement for an ion storage layer, self-coloring, and returning the energy consumed for deintercalation of the guest ions. Typically an electrochromic battery is a “sandwich” structure that contains substrate, transparent conductor, ion conductor, anode (usually a metal) and electrochromic layer (the most important part), as shown below in Figure 2-5.

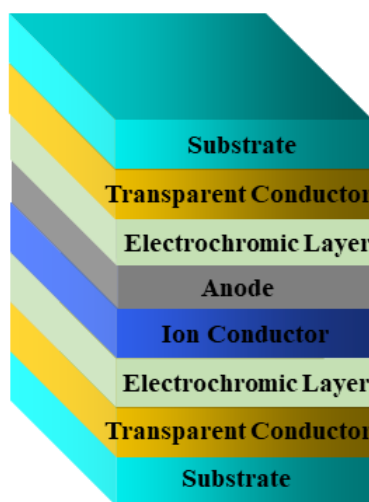


Figure 2-5. Structure of a typical electrochromic battery.

2.4 Methods of Electrochromic Films Preparation

Electrodeposition Method

Electrodeposition is a process where one takes advantage of the electrical conductivity of molecules (or ions) in solution to deposit the molecules (or ions) on a conductive electrode. As shown in Figure 2-6, by applying alternating voltage, molecules (or ions) are deposited on the electrode (normally ITO or FTO glass).^[23] The electrochromic films created by electrodeposition are typically composed of coalesced amorphous nanoparticles, which provide a large electrode surface area and short solid-phase ion diffusion pathways.

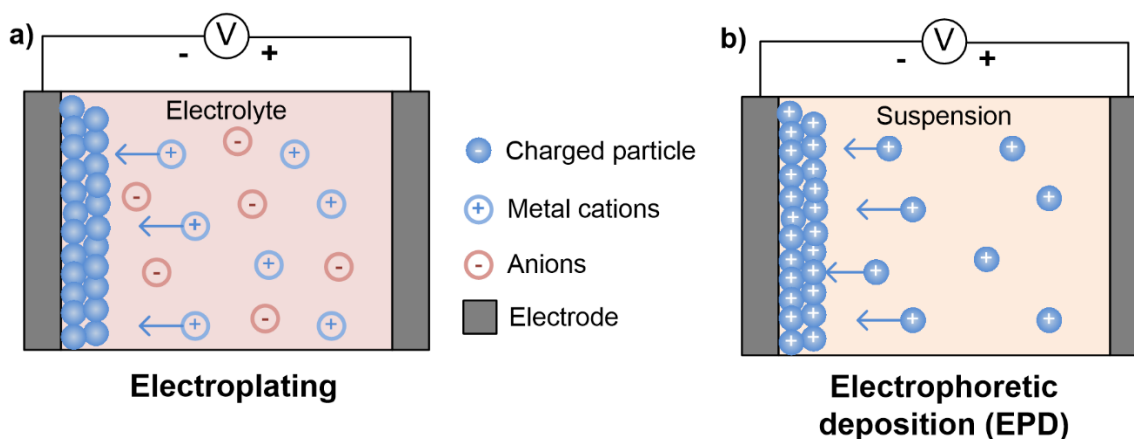


Figure 2-6. Schematic representation of the two types of cathodic electrodeposition processes: (a) electroplating and (b) electrophoretic deposition (EPD). Reprinted from Ref. [23]. Copyright 2015, IntechOpen.

Hydrothermal Method

The hydrothermal method is a method of synthesis of crystallizing substances from high-temperature aqueous solutions at high vapor pressures. It has the advantages of being low cost and controllable. An example of TiO_2 nanoparticle preparation is shown below (Figure 2-7).^[24]

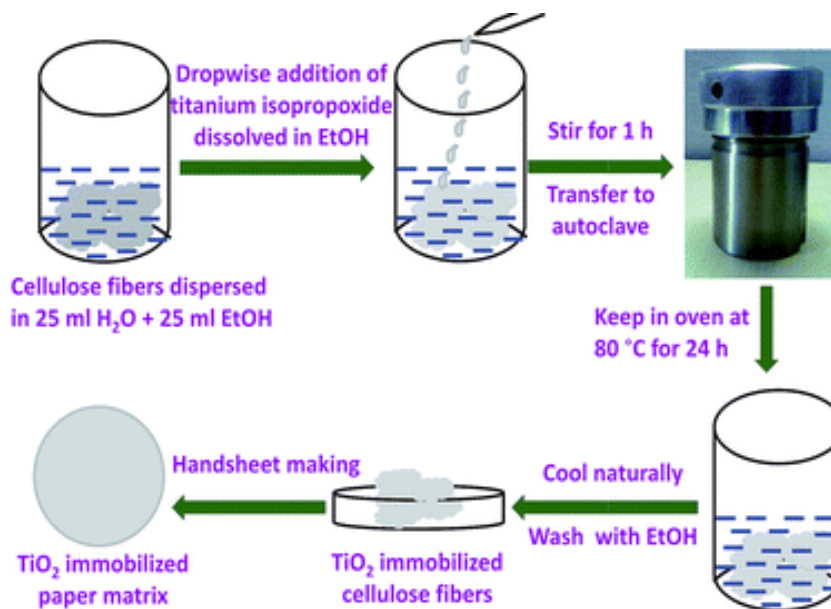


Figure 2-7. Schematic representation of the immobilization of TiO_2 nanoparticles on the surface of cellulose fiber of the paper. Reproduced from Ref. [24] with permission from The Royal Society of Chemistry.

Spray Coating Method

The spray coating method involves spraying a solution to the substrate through a nozzle. For the formation of a uniform layer, the solutions must have very low viscosity. This method is widely employed since it is compatible with large-scale electrode fabrication and can coat at high speed. An illustration of the spray coating method is shown below (Figure 2-8).^[25]

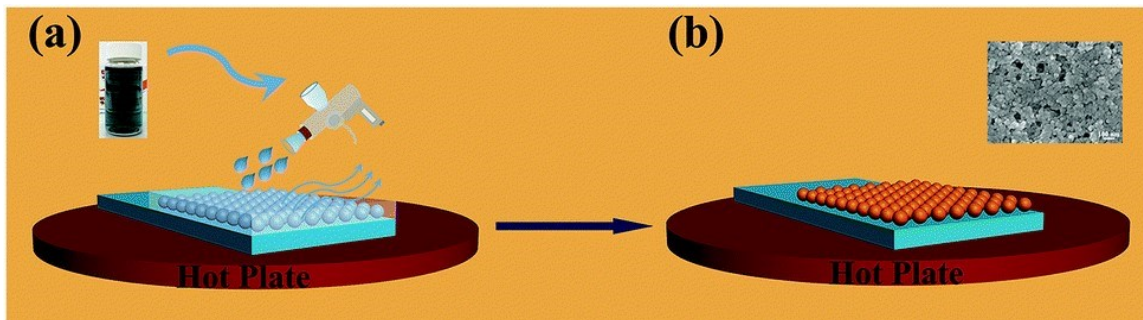


Figure 2-8. (a) Pale blue solution is sprayed onto FTO glass. (b) Coated substrate is dried and oxidized subsequently as the droplet is sprayed onto the hot FTO glass. Reproduced from Ref. [25] with permission from The Royal Society of Chemistry.

Inkjet Printing Method

The inkjet printing method involves the coating application of a solution to a substrate. This method is used in constructing flexible devices; therefore, inkjet printing plays an important role in transistors and light-emitting devices fabrication.^[26] Electrochromic layers can also be built using this deposition method. The inkjet printing method is a precise coating technology having the following advantages: low cost, high-resolution pattern fabrication, and highly efficient material use.

2.5 Parameters of Electrochromism

Color and Transmittance

The visible light spectrum is the range of light that a human eye sees. The wavelengths range from 380 to 700 nm and are separated into the color bands of the rainbow because each color is a different wavelength. Table 2-1 shows the color of light under different wavelengths.

Table 2-1. Wavelength for color bands in a visible light spectral region.

Color band	Wavelength (nm)
Red	620-750
Orange	590-620
Yellow	570-590
Green	495-570
Blue	450-495
Violet	380-450

The transmittance of a smart window is defined as the fraction of incident electromagnetic power that is transmitted through the window. The degree of optical contrast of transmittance during the reversible color-switching process indicates the electrochromic performance of smart windows.

Coloration efficiency

A key metric of electrochromism is coloration efficiency (CE), which represents the change in optical density (ΔOD) per unit of charge intercalated into the electrochromic layer, as represented by Equation 2.3.^[28]

$$\Delta OD = \log(T_c/T_b) = \eta Q/A \quad (2.3)$$

where η is coloration efficiency (CE), Q is charge (C), A is contact area (cm^2), T_c and T_b are the transmittances of electrochromic devices at coloration and bleaching states, respectively.

Response time

Response time reflects the switching time (time for color change) required for electrochromic devices. The response time is defined as the time required to achieve 90% of the maximum optical contrast.^[29]

Cycle performance

Cycle performance is a key metric of smart windows. Normally, 10^5 times of cycles are required for the practical application of smart windows.

2.6 Discussion

In this chapter, the critical components and the system of electrochromism are discussed. Electrochromic material can be classified into inorganic and organic material. Inorganic material includes cathodic material and anodic material. WO_3 is the most widely used cathodic material and NiO is the most widely used anodic material. Organic materials are often known as conductive polymers and bipyridine-based compounds. Electrochromic material can be used to create electrochromic devices, which are composed of substrate, transparent conductor, counter-electrode (or anode), electrochromic layer, and ion conductor. Since electrochromic material can reversibly change their optical properties

under an applied voltage which adjusts the light transmittance and solar radiation of smart windows, the energy loss caused by the temperature difference (between indoor temperature and outdoor temperature) will be reduced. Some methods for the preparation of electrochromic layers were presented: electrodeposition, hydrothermal, spray coating, and inkjet printing methods. The parameters of electrochromism include color and transmittance, coloration efficiency, response time, and cycle performance. In summary, the following problems should be solved for the development of smart windows:

(1) The operation of traditional electrochromic devices requires external voltages to trigger the coloration/bleaching processes, which makes the traditional electrochromic device far from a net-zero energy-consumption technology. It is necessary to develop energy-efficient electrochromic smart windows.

(2) The solution-processed approach is compatible with large-scale electrode fabrication and high-speed production, thus making it promising for practical thin film fabrication. A simple, scalable method for synthesizing aqueous nanoparticle inks is needed.

Problem (1) is addressed by electrochromic supercapacitors and electrochromic batteries (Chapters 3 and 4). Problem (2) is addressed by synthesizing aqueous nanoparticle inks (Chapter 4).

Chapter 3

Oxygen Vacancy Tunable Electrochemical Properties of Electrodeposited Molybdenum Oxide Films

A version of this Chapter has been published in ACS Applied Materials&Interfaces:

Zhang, W.; Li, H.; Firby, C. J.; Al-Hussein, M.; Elezzabi, A. Y. Oxygen-Vacancy-Tunable Electrochemical Properties of Electrodeposited Molybdenum Oxide Films. *ACS Appl. Mater. Interfaces* **2019**, 11, 20378–20385.

(DOI: 10.1021/acsami.9b04386)

3.1 Introduction

Alternative energy sources and multifunctional energy storage devices have attracted much research interest for the demand of renewable energy and energy saving. Among various energy saving strategies, electrochromic devices and hydrogen evolution reaction (HER) are thought to be promising methods for the development of environment-friendly devices. An electrochromic device (ECD), where ions are injected into electrochromic layer during charging and whereas, during discharging, ions move backward to ions storage layer, show great promise in green building to decrease the cost of air conditioning and sun shading, and simultaneously improve the indoor living comfort.^[30] On the other hand, HER is being utilized to generate hydrogen gas for next generation clean energy fuel.^[31] To date, noble metal, such as Platinum (Pt) is shown to be most the efficient catalyst with low overpotential

and high current for HER.^[32] However, the high cost and shortage of noble metal sources limit its application.

For the development of the above technologies, material properties play an important role. Transition metal oxides (TMOs) have shown great potential for low-cost and environmentally-friendly energy storage/conversion technologies due to their remarkable multivalence states and the associated redox reactions.^[33,34] Molybdenum oxides, a typical kind of TMO, have been identified as an emerging choice for a variety of applications, such as supercapacitors,^[35,36] hydrogen evolution reactions (HER),^[37] batteries,^[38,39] and electrochromic devices (ECDs).^[40,41] However, the low electrical conductivity and slow reaction kinetics of MoO₃, where Mo is in its highest oxidation state, prevent the widespread use of MoO₃ in such applications.^[42,43] In recent years, the introduction of oxygen vacancies has been found to mediate these drawbacks. The oxygen vacancies are found to serve as shallow donors and enhance charge carrier mobility, thus improving the electrical conductivity.^[44,45] Techniques, such as extrinsic N doping,^[46] radio-frequency (RF) magnetron sputtering,^[47] solvothermal, and vacuum sublimation method (where strict heat treatment and vacuum environment are required for obtaining sub-stoichiometric molybdenum oxides),^[48,49] were used to introduce oxygen vacancies in MoO₃. However, these methods hinder the widespread utilization of MoO₃ due to their elaborate material processing and stringent parameters control needed for high yield.

Compared to the aforementioned methods, electrodeposition provides several unique advantages, including control over the film's layer thickness, large scale scalability, low reaction temperatures, and cost-effectiveness. Most importantly, the electrodeposited films are typically composed of coalesced amorphous nanoparticles, which provide large

electrode surface area and short solid-phase ion diffusion pathways. Notably, these characteristics result in high electrochemical performance.^[50–53] Furthermore, the electric field applied during electrodeposition process not only binds the target material to the substrate,^[54] but also introduces oxygen vacancies, thus, altering the valence state of the film's constituent materials.^[55,56] For example, the electrodeposition of In_2O_3 and MnO_2 were shown to introduce oxygen vacancies and alter the valence state, resulting in improved electrochemical performance.^[57,58]

It has previously been reported that nanoscale TMOs can be prepared from chemical precursor solution via electrodeposition.^[58–61] However, the introduction of oxygen vacancies into nanoscale TMOs material, and the resulting effect on their electrochemical performance has yet to be extensively explored. Herein, we utilize electrodeposition to form a MoO_3 nanoparticle colloid onto indium tin oxide (ITO)-coated glass to show that the reduction of the valence of Mo (VI) to Mo (IV, V) and the formation of a thin MoO_{2+x} film yields an enhanced super-capacitive performance. The electrodeposited MoO_{2+x} electrode exhibits an areal capacitance of 89 mF cm^{-2} at 1 mA cm^{-2} , and a negligible capacitance loss within 600 cycles. Additionally, the MoO_{2+x} films possess a high diffusion coefficient for H^+ ions needed for intercalation ($3.30 \times 10^{-8} \text{ cm}^2 \text{ s}^{-1}$) and deintercalation ($1.80 \times 10^{-8} \text{ cm}^2 \text{ s}^{-1}$). This enhanced super-capacitive performance makes these electrodeposited MoO_{2+x} films highly promising candidates as counter electrodes in complementary ECDs. As such, in comparison to single-active-layer ECD, the introduction of MoO_{2+x} electrode accelerates the redox reactions at the working electrode. We show that the coloration potential of the complementary ECD decreases to -0.5 V and the bleaching potential reaches as low as 0.5 V . We further investigate the HER catalysis activity of MoO_{3-y} where Mo is in V and VI

valence states. After annealing the electrodeposited MoO_{2+x} film at 200 °C for 24 hours, MoO_{2+x} can be partially oxidized to MoO_{3-y} and exhibits high catalysis activity for HER. The MoO_{3-y} electrode shows an overpotential of 201 mV at current density of 10 mA cm^{-2} with a Tafel slope of 90 mV. Interestingly, upon annealing the MoO_{2+x} film at 300 °C for 6 hours, the Mo reaches its highest oxidation state (VI), and the resulting MoO_3 film exhibits a battery-like characteristics.

3.2 Experimental Section

Materials

All the chemicals were analytical grade and were used without further purification. Molybdenum powder (Mo, 99.99%), tungsten powder (W, 99.99%), sulfuric acid (H_2SO_4 , 98%), and polyvinyl alcohol (PVA, Mw ~130,000) were acquired from Sigma-Aldrich. Nitric acid (HNO_3 , 68%) was acquired from Fisher. Hydrogen peroxide (H_2O_2 , 30%) was acquired from ACS reagent.

Synthesis of MoO_3 Colloid

The MoO_3 colloid was prepared according to our previous protocol.^[30] Briefly, Mo powder (0.36 g) was added to 75 mL of HNO_3 solution (0.5 M) and refluxed at 75 °C under stirring for five hours to form a solution with a white suspension composed of $\text{MoO}_3 \cdot 0.5\text{H}_2\text{O}$ and $\text{MoO}_3 \cdot \text{H}_2\text{O}$. The white suspension was collected by centrifugation and washed with deionized (DI) water six times. Next, the product was diluted by DI water to form a precursor solution (1.5 mg mL^{-1}). The precursor solution was then sonicated in an ultrasonic bath (Edmund Scientific Co., Barrington, NJ) until a clear solution was formed.

Electrodeposition of MoO_{2+x} Films

Prior to the deposition, ITO-coated glass (3 cm×4 cm) substrates were cleaned with ethanol and deionized (DI) water. A 2 cm×2 cm area of the ITO film was removed from the substrate, via laser ablation, to create a non-conductive region on the glass substrate (See Figure A-1). A three-electrode configuration was used to electrodeposit MoO_{2+x} films, with Pt wire, ITO glass, and Ag/AgCl as the counter, working and reference electrodes, respectively. The MoO₃ colloid was electrodeposited onto an effective 3×3 cm² area of the ITO glass substrate at a pulsed (1 second) current of -0.3 mA cm^{-2} and a pulsed (3 seconds) 0.03 mA cm^{-2} for 1,200 cycles, to obtain the MoO_{2+x} film. MoO_{3-y} and MoO₃ films were prepared by annealing in ambient air the MoO_{2+x} electrodes at 200 °C for 24 hours and 300 °C, respectively, for six hours.

Electrodeposition of WO₃ Films

W powder (1.8 g) was added to 60 mL of H₂O₂ solution (30%) and stirred for 12 hours to form a yellow peroxotungstic acid colloid. Next, the sediments were filtered to obtain a clear colloid. The clear colloid was electrodeposited onto pre-cleaned ITO-on-glass substrate (3×3 cm²) at -0.3V for 180s to obtain a WO₃ electrode.^[62,63]

Electrochromic Device Assembly

The complementary ECD was assembled using the MoO_{2+x} electrode as the counter electrode, the WO₃ electrode as the working electrode, and PVA-H₂SO₄ as the electrolyte. The single-active-layer ECD was constructed using ITO-on-glass as the counter electrode, the WO₃ electrode as the working electrode, and PVA-H₂SO₄ as the electrolyte. The solid state PVA-H₂SO₄ electrolyte was prepared based on previous report.^[16] 6 g of PVA was gradually added to 60 mL H₂SO₄ solution (1 M) at 85 °C under stirring. When the mixture

became transparent, the prepared electrodes were immersed into the hot electrolyte for 10 seconds.

Characterization

X-ray photoelectron spectroscopy (XPS) (Kratos AXIS Ultra), transmission electron microscope (TEM) (JEM-ARM200CF, JEOL) and field emission scanning electron microscopy (FE-SEM) (Zeiss SIGMA FESEM, German) were used to analyze the composition and structure of samples. Electrochemical measurements were carried out using a Zahner electrochemical workstation (Zennium CIMPS-1). A three-electrode configuration was used for electrochemical measurements with Pt wire and Ag/AgCl as counter and reference electrodes in a 0.5 M H₂SO₄ solution. Electrochemical impedance spectroscopy (EIS) analysis was conducted by applying an AC voltage of 10 mV over a frequency range between 0.1 Hz and 100 kHz. The linear sweep voltammetry (LSV) of hydrogen evolution reaction (HER) were Internal Resistance-corrected based on reversible hydrogen electrode (RHE), and internal resistance of electrodes was obtained from the EIS measurements (Figures S3-2 and S3-3). LSV was conducted in a 0.5M H₂SO₄ solution at a scan rate of 5 mV s⁻¹. The long-term stability is assessed by taking continuous cyclic voltammograms at a scan rate of 50 mV s⁻¹ for 800 times. An Ocean Optics USB4000 spectrometer was used to measure the optical wavelength transmission. No background correction was applied to the spectra. The dynamic characterizations were conducted by directing a helium neon laser (wavelength of 632.8 nm) through a quartz cell ECDs. The voltage was applied from Zahner and the photodiode output signal was collected with an oscilloscope. The response time is calculated based on 90% transmittance change.

The areal capacitance (C_A) is calculated according to:

$$C_A = \frac{I}{A} \left(\frac{\Delta t}{\Delta V} \right) \quad (3.1)$$

where I is the discharge current, Δt is the discharge duration, A is geometrical area of each film and ΔV is the discharge potential window.

3.3 Results and Discussion

The electrodeposited MoO_{2+x} films are imaged by scanning electron microscopy (SEM) and transmission electron microscope (TEM). As shown in Figures 3-1a and 3-1b, the MoO_{2+x} electrode exhibits a uniform nanoparticle film, confirming the colloidal electrodeposition of nanoparticle films. The inset TEM image in Figure 3-1b confirmed the nanoparticles size is approximately 20nm. To evaluate the valence state of Mo in MoO_{2+x} films, XPS was carried out. In Figure 3-1c, the XPS survey spectrum indicates the presence of both Mo and O elements. Furthermore, the high resolution XPS Mo 3d core level spectrum is shown in Figure 3-1d, where the most intense duplet peaks are located at 230.2 eV and 233.4 eV. These are the binding energy of electrons in $3d_{5/2}$ and $3d_{3/2}$ levels of Mo in Mo (IV) valence state.^[64] Another pair of peaks, located at 231.6 eV and 234.8 eV, are attributed to Mo (V).^[65] The atomic ratio of Mo (IV) and Mo (V) is estimated to be 1.56 (Table A-1), which indicates that $x \approx 0.20$. It should be noted that both Mo (IV) and Mo (V) oxidation states contribute to oxygen vacancies in MoO_{2+x} film. These oxygen vacancies are introduced in electrodeposited MoO_{2+x} films due to the assistance of external negative electrical field.

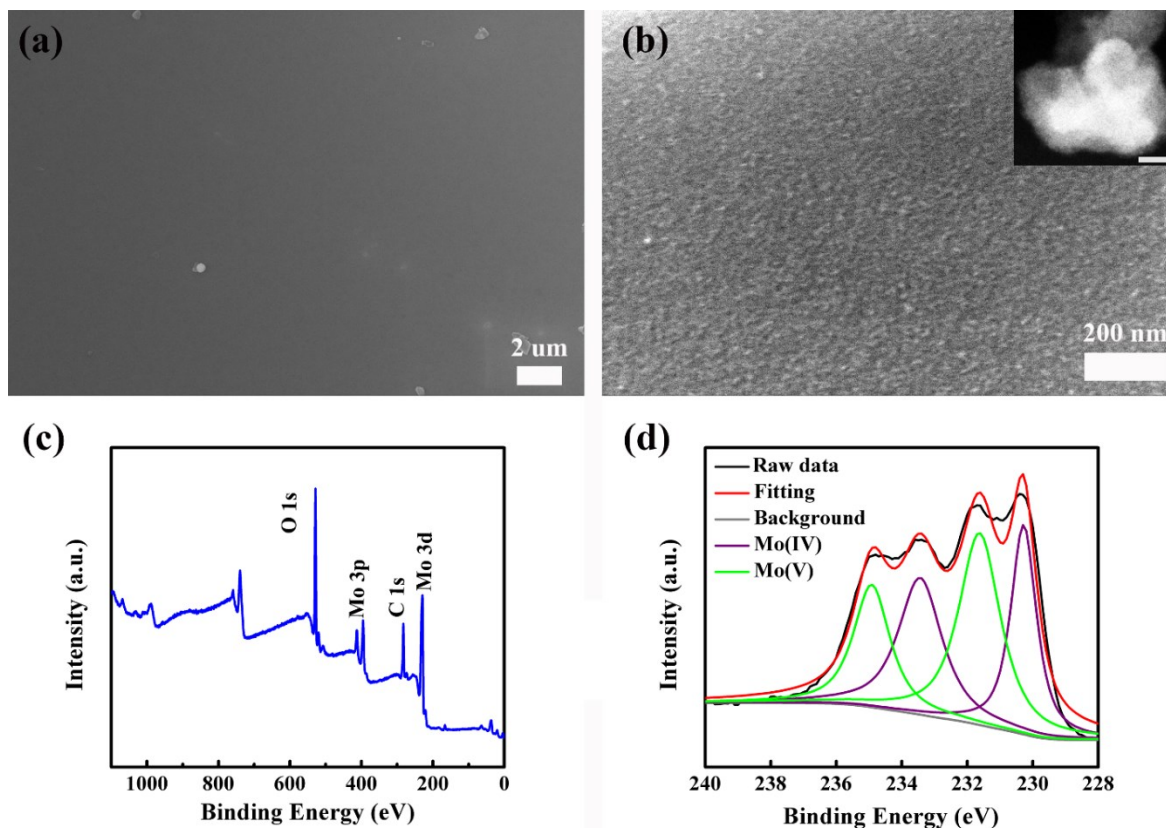


Figure 3-1. FESEM images of prepared MoO_{2+x} nanofilms with (a) low magnification and (b) high magnification. Inset in (b) is a DF-STEM image showing MoO_{2+x} nanoparticles (scale bar: 20 nm). (c) XPS survey spectrum of MoO_{2+x} . (d) The Mo 3d XPS spectrum of MoO_{2+x} .

Figure 3-2a depicts the cyclic voltammetry (CV) curves of the MoO_{2+x} nanofilm in a 0.5 M H_2SO_4 solution measured at different scan rates. Here, the diffusion coefficient of H^+ for intercalation and deintercalation can be estimated according to the measured peak current, I_p (Amps),^[66]

$$I_p = 2.69 \times 10^5 AC \sqrt{Dvn^3} \quad (3.2)$$

where n is the number of electrons transferred (assumed to be 1), A is contact area (cm^2), D is the diffusion coefficient of the H^+ ions ($\text{cm}^2 \text{s}^{-1}$), C is the concentration of the H^+ ions

in electrolyte solution (mol cm^{-3}), and v is the scan rate (V s^{-1}). The peak current density of intercalation/deintercalation as a function of the square root of scan rates is shown in Figure 3-2b. Accordingly, the diffusion coefficients of H^+ for intercalation and deintercalation are calculated to be $3.305 \pm 0.015 \times 10^{-8} \text{ cm}^2 \text{ s}^{-1}$ and $1.800 \pm 0.017 \times 10^{-8} \text{ cm}^2 \text{ s}^{-1}$, respectively. Remarkably, the diffusion rate of H^+ in MoO_{2+x} films are 10^4 times faster to the previously reported diffusion coefficient of H^+ for intercalation in a $\alpha\text{-MoO}_3$ supercapacitor ($\sim 3.32 \times 10^{-12} \text{ cm}^2 \text{ s}^{-1}$).^[67] This enhanced diffusion rate is attributed to the improved electrical conductivity of coalesced amorphous nanoparticles film. To further understand the electrochemical behaviour of this electrode, the galvanostatic charge/discharge processes were measured under different current densities. As shown in Figure 3-2c, the charging and discharging time are approximately equal for all the charge-discharge curves, resulting in excellent energy storage and release circle. By examining the Nyquist plot (Figure A-2), the short Warburg region confirms the high of H^+ diffusion coefficient for the intercalation and deintercalation processes. At low frequency region of EIS, the steep slope indicates that the MoO_{2+x} film is a highly-promising material for supercapacitive applications.^[68] This is further supported by calculation the areal capacitance as shown in Figure 3-2d where it ranges from 89 mF cm^{-2} to 2.5 mF cm^{-2} as the current density varies from 1 mA cm^{-2} to 5 mA cm^{-2} . Remarkably, the areal capacitance of 89 mF cm^{-2} is 3.56 times higher than that of a carbon fiber/ MoO_3 (i.e. 25 mF cm^{-2} at 1 mA cm^{-2}) material,^[69] suggesting the excellent ion storage capability of the MoO_{2+x} film. The areal capacitance of MoO_{2+x} films decreases with the increase of current density, which can be explained by insufficient ion transfer at the electrode/electrolyte interface at high current density. Nonetheless, even at 5 mA cm^{-2} , the areal capacitance of 2.5 mF cm^{-2} , is

still higher than the previously reported value of $\sim 2 \text{ mF cm}^{-2}$.^[70] Along with the excellent ion storage capability, the MoO_{2+x} films also possess excellent cycling stability with negligible capacitance loss within 600 cycles (Figure A-4).

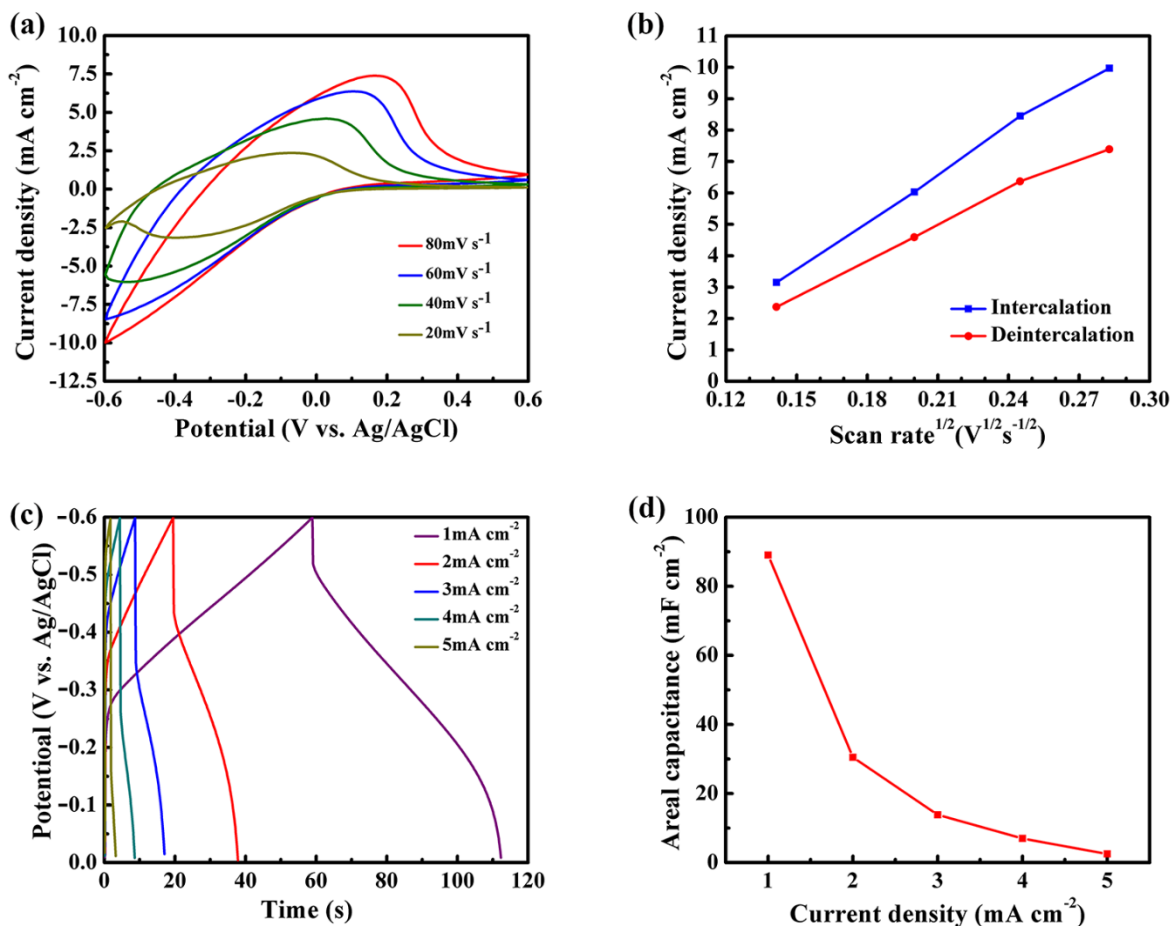


Figure 3-2. (a) CV curves of MoO_{2+x} at different scan rates in a 0.5 M H_2SO_4 solution. (b) Peak current density of intercalation/deintercalation as a function of the square root of scan rates (c) Charge-discharge curves of MoO_{2+x} at various current densities. (d) The areal capacitance of the MoO_{2+x} films.

Interestingly, the MoO_{2+x} , having such enhanced ion storage properties, can be used as a counter electrode in a complementary ECD. A prototype device ($3 \text{ cm} \times 3 \text{ cm}$) was assembled (see Experimental section), where a MoO_{2+x} electrode serves as the counter

electrode for storing ions, and a WO_3 electrode serves as the working electrode. The opposing redox reactions occur at the electrodes in a complementary ECD, while the WO_3 electrode is being oxidized (bleaching) or reduced (coloring), the MoO_{2+x} electrode can be simultaneously reduced or oxidized at the counter electrode. The high diffusion rate of MoO_{2+x} electrode enhances this process. In a single-active-layer ECD, ITO film serves as the counter electrode, but it has poor charge storage properties.^[71] This indicates that the poor redox reactions at the counter electrode would hinder the electrochemical kinetics of the device, leading to a higher operating voltage for the device. Images of the complementary ECDs (top) and single-layer-active ECDs (bottom) under different voltages are shown in Figure 3-3a. Following the images in Figure 3-3a from left to right, both the complementary and the single-active-layer ECDs are colored under no bias (pristine), -0.5 V, -1.5 V, -2 V and -2.5 V biases for 5 min, respectively. For complementary ECD, the color change can be noticed at a low applied voltage of -0.5 V, while the color change appears above -2 V for single-active-layer ECD. Clearly, the introduction of the MoO_{2+x} electrode lowers the activation voltage of the ECD from -2 V to -0.5 V. This improvement indicates that MoO_{2+x} film can accelerate redox reactions at the working electrode, thus leading to reduced potential of hydrogen ion insertion into the WO_3 film.

For more detailed optical analysis, the transmittance contrast of the complementary ECD is measured to be 23% at 632.8 nm under -0.5 V (Figure 3-3b), while the contrast of single-active-layer is undetectable at -0.5 V (Figure 3-3c). At a voltage of -1.5 V, the transmittance contrast of complementary ECD reaches 38% at 632.8 nm, whereas the contrast of single-active-layer ECD is still negligible under -1.5 V. Compared to the 47% transmittance contrast of complementary ECD, under -2 V the single-active-layer ECD just

starts coloration with 19% optical contrast. Moreover, the complementary ECD reaches 63% contrast at 632.8 nm under -2.5 V, which is 6% higher than the contrast of single-active-layer ECD at the same applying voltage. The lower activation voltage of the complementary ECD indicates faster diffusion kinetics compared to the single-active-layer ECD.

The dynamic transmittance characterization of the ECD at 632.8 nm is presented in Figure 3-3d. The complementary ECD can achieve a fully-cycled color change at -2.5 V (coloration) and 0.5 V (bleaching), while single-active-layer ECD cannot reach fully bleached state at 0.5 V. Since the MoO_{2+x} speeds up the hydrogen ion transport kinetics of the ECD, the complementary device shows a faster switching speed. The response times of the complementary ECD is calculated to be 24.2 s for coloration and 32 s for bleaching, whereas the single-active-layer device colors at 28s and bleaches at 46 s. Furthermore, the complementary ECD also exhibits higher energy storage compared to the single-active-layer ECD. In Figure 3-3e, the discharging time of complementary device indicates a capacity of 3.3 mF cm^{-2} at 0.1 mA cm^{-2} , compared to 0.7 mF cm^{-2} in the single-active-layer device. Remarkably, this areal capacity of complementary ECD is also higher than previously observed capacity of WO_3 ($\sim 1 \text{ mF cm}^{-2}$),^[72] suggesting higher energy storage with the assistance of MoO_{2+x} electrode. Moreover, a key metric of ECDs is coloration efficiency (CE) which represents the change in optical density (ΔOD) per unit of charge intercalated into the electrochromic layer. The CE of the complementary ECD achieves $61.2 \text{ cm}^2 \text{ C}^{-1}$ (Figure 3-3f), which is higher than the $54.8 \text{ cm}^2 \text{ C}^{-1}$ of single-active-layer ECD (Figure 3-3g), indicating the complementary ECD is more efficient and promising for electrochromic applications.

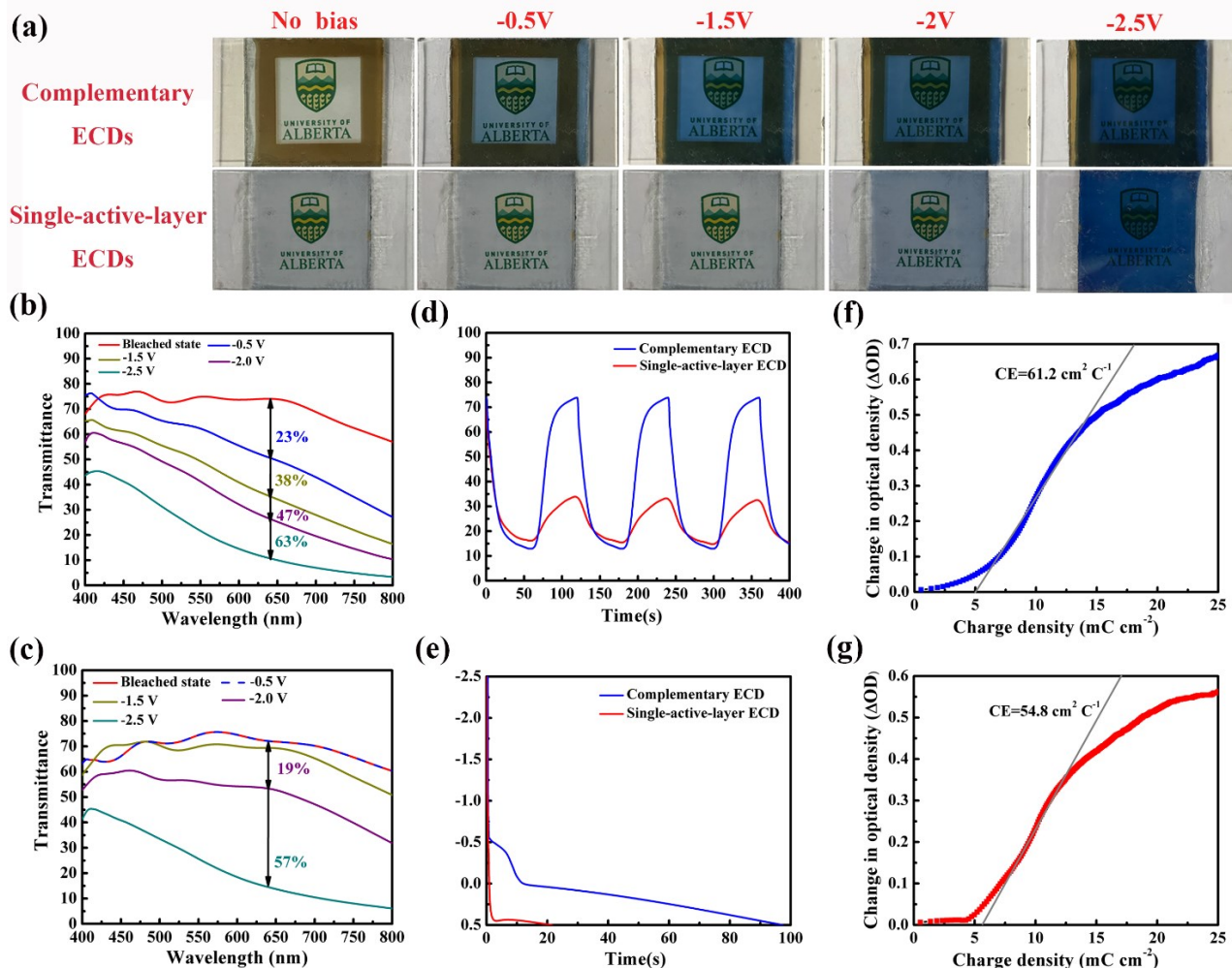


Figure 3-3. (a) Digital photographs of ECDs under different voltages. From left to right, both complementary (top) and single-active-layer (bottom) ECDs are charged under no bias (pristine), -0.5 V, -1.5 V, -2 V and -2.5 V biases for 5 min. (b) Visible transmittance of complementary ECD under various voltages. (c) Transmittance contrast of single-active-layer ECD under various voltages. (d) In-situ transmittance spectrum of the complementary ECD and single-active-layer ECD under -2.5 V (coloring) for 60 seconds and 0.5 V (bleaching) for 60 seconds, alternately, applied potentials at an optical wavelength of 632.8 nm. (e) Discharge curves of single-active-layer ECD and complementary ECD at a current density of 0.1 mA cm⁻². (f) CE of complementary ECD and (g) single-active-layer ECD under -2.5 V applied potential for the optical wavelength of 632.8 nm.

While the MoO_{2+x} can be utilized as a supercapacitor electrode with superior ion storage, MoO_{3-y} is also an efficient electrocatalyst for HER.^[73–76] To demonstrate such functionality, then we partially oxidized the electrodeposited MoO_{2+x} to MoO_{3-y} under a temperature of 200 °C and evaluated the HER catalytic activities of MoO_{3-y} and MoO_{2+x} electrodes. As shown in Figure 3-4a, a uniform nanoparticle surface that is consistent with MoO_{2+x} film was observed, indicating the MoO_{2+x} film can be oxidized under 200 °C without obvious morphology change. The valence state of Mo was investigated by XPS spectra. In Figure 3-4b, the high resolution XPS Mo 3d core level spectrum shows the coexistence of Mo (V) and Mo (VI), indicating the transformation of MoO_{2+x} (VI, V) to MoO_{3-y} (V, VI). The atomic ratio of Mo (V) and Mo (VI) is estimated to be 1.08 (Table A-1), which indicates that $y \approx 0.26$. The HER catalysis was measured in a N_2 -saturated 0.5 M H_2SO_4 solution with a three-electrode configuration. For comparison, measurements in the same conditions were performed on a bare ITO-on-glass substrate, and a MoO_{2+x} electrode. The linear sweep voltammetry (LSV) curves of different samples are shown in Figure 3-4c. The MoO_{3-y} electrode shows an overpotential of 201 mV (vs. RHE) to achieve the standard HER current density of 10 mA cm^{-2} , while the LSV curves of bare ITO-on-glass substrate and MoO_{2+x} electrode are flat and cannot reach the standard HER current density of 10 mA cm^{-2} (within 250 mV overpotential). Thus, the HER catalytic properties of bare ITO-on-glass substrate and MoO_{2+x} electrode are negligible, indicating that the MoO_{2+x} electrode can be utilized in a complementary ECD without electrolyte splitting. The mechanism and kinetics of the HER performance of MoO_{3-y} electrode is further investigated by Tafel slope. The Tafel slope is derived from the LSV curve by fitting experimental data near onset potential to the equation $\eta = a + b \log(j)$, where η is overpotential, b is Tafel slope, and j is current density.^[77]

A Tafel slope of 90 mV per decade is obtained for MoO_{3-y} electrode. The rate of HER is controlled by a high Tafel slope step (Volmer step ~ 120 mV per decade) and a low Tafel slope step (Heyrovsky step ~ 40 mV or Tafel step ~ 30 mV per decade). Volmer step indicates the proton adsorption onto active site, while Heyrovsky or Tafel step indicates the evolution of hydrogen molecule from catalyst surface.^[78] A Tafel slope of 90 mV per decade suggests the dominant HER step of MoO_{3-y} film is Volmer step. The Tafel slope of 90 mV per decade is less than the value of previously reported bulk $\alpha\text{-MoO}_3$ (122 mV per decade), indicating a faster HER catalytic rate.^[74] Moreover, the overpotential of the MoO_{3-y} electrode is only slightly increased to 216 mV after 800 cycles (Figure 3-4d), indicating its good stability. Furthermore, to demonstrate a fully cycle of oxygen vacancies recovery, MoO_3 films with obvious morphology change are prepared (Figures A-5a and A-5b) after annealing MoO_{2+x} electrodes under 300 °C in ambient air. The CV curve of the MoO_3 film demonstrates clear redox peaks (Figure A-5c), revealing that the elimination of oxygen vacancies enables the MoO_3 to be a promising battery electrode.

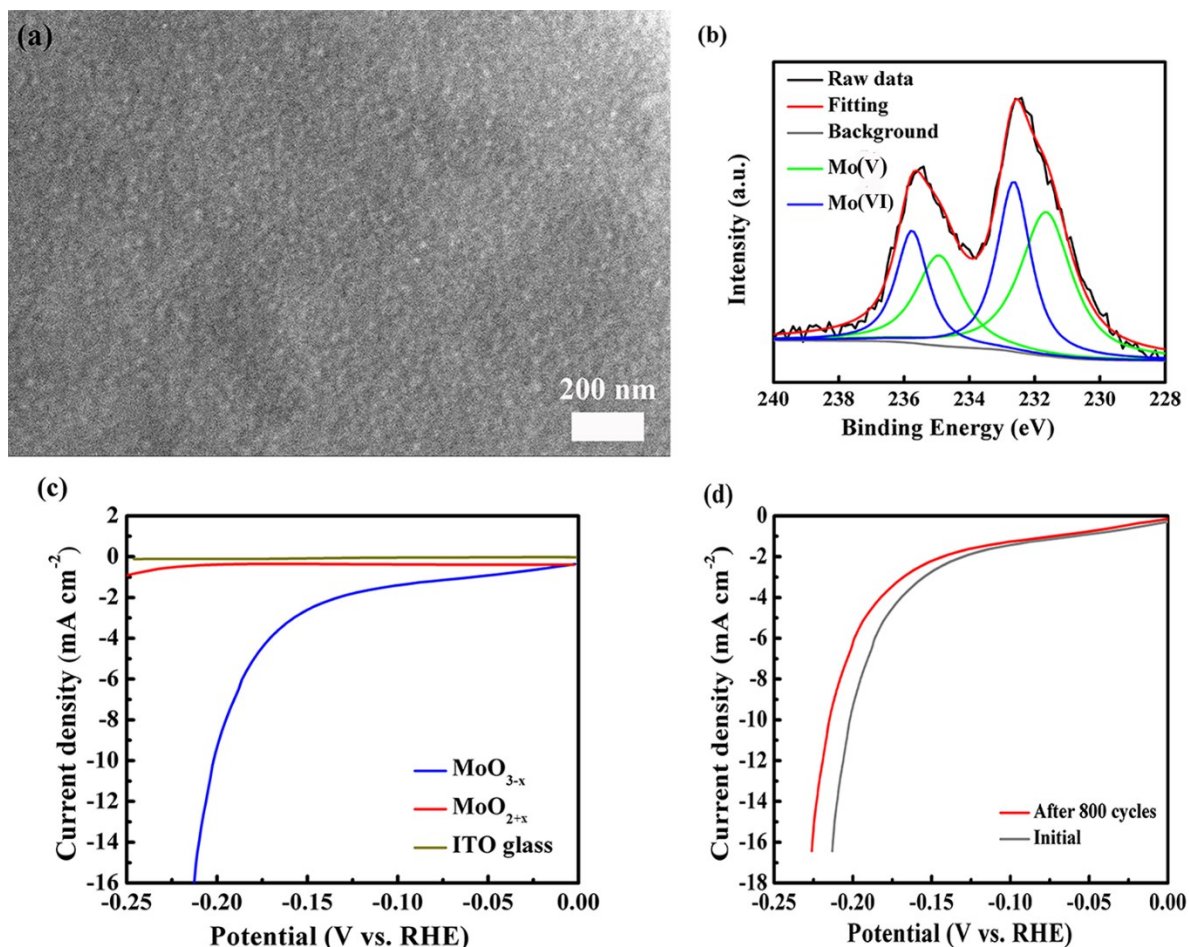


Figure 3-4. (a) FESEM image of as prepared MoO_{3-y} nanofilms. (b) Mo 3d XPS spectrum of MoO_{3-y} . (c) LSV curves of bare ITO glass, MoO_{2+x} and MoO_{3-y} electrodes at a scan rate of 5 mV s^{-1} . (d) Durability test for the MoO_{3-y} catalyst after 800 cycles.

3.4 Summary

We present a novel colloidal electrodeposition method for fabricating molybdenum oxide films with oxygen vacancies. We fabricated MoO_{2+x} electrodes that exhibit superior supercapacitive performance with an areal capacitance of 89 mF cm^{-2} at 1 mA cm^{-2} . The MoO_{2+x} electrode can be utilized as a counter electrode for in complementary ECDs. The complementary ECD remarkably lowered the activation potential for coloring and

bleaching, which can be colored at -0.5 V while the single-active-layer ECD shows no color change at this bias. The complementary ECD also exhibits a high areal capacitance and fast switching performance. Moreover, we demonstrated that the oxidization of MoO_{2+x} can achieve molybdenum oxide with different valences (V, VI) that exhibit different electrochemical characteristics. When annealing the MoO_{2+x} under 200 °C, MoO_{2+x} can be partially oxidized to MoO_{3-y} , which can be used for efficient electrocatalytic hydrogen evolution reaction. When fully oxidized to MoO_3 , the electrode exhibits a battery feature. This new and facile strategy to fabricate sub-stoichiometric molybdenum oxide nanofilms reveals the effect of different valences (IV, V and VI) on the electrochemical performance of the molybdenum oxide films and has the potential to be applied to other transition metal oxides.

Chapter 4

Electrochromic Battery Displays with Energy Retrieval Functions Using Solution-Processable Vanadium Oxide Inks

Zhang, W.; Li, H.; Al-Hussein, M.; Elezzabi, A. Y. Electrochromic Battery Displays with Energy Retrieval Functions Using Solution-Processable Vanadium Oxide Inks. *Advanced Optical Materials* **2020**, 8, 1901224.

(DOI: 10.1002/adom.201901224)

4.1 Introduction

Given the demand for efficient energy technology, electrochromic devices have attracted much research interest.^[81] Among their various applications, electrochromic displays, still in the incipient development stage, show significant promise for developing bistable displays due to their zero-energy consumption while maintaining a colored or colorless state.^[82] However, operation of traditional electrochromic displays requires external voltages to trigger the coloration/bleaching processes, which makes the traditional electrochromic displays far from a net-zero energy-consumption technology. The majority of electrochromic display research has focused on developing nanostructure electrochromic materials for fast switchings^[83,84] without paying attention to how to reduce the consumed energy of the electrochromic displays.

Recently, we developed a promising Zn-based electrochromic battery technology for smart

windows.^[39] The electrochromic battery exhibits self-coloration behaviors and eliminates the external voltage requirement for triggering the coloration process. The aqueous compatible Zn anode implements a much lower charged/bleached voltage for the electrochromic battery compared to the Li- and Al-based electrochromic batteries.^[85,86] The lower charged/bleached potential indicates a lower energy consumption during the bleaching process. As such, the Zn-based aqueous electrochromic battery platform is an energy-efficient technology for reducing the energy consumption of electrochromic devices. To date, no reports exist on the utilization of electrochromic battery systems for developing energy-efficient electrochromic displays.

Electrochromic materials play an important role in the development of electrochromic battery displays. Transition metal oxides (TMOs) have shown excellent electrochromic properties due to their remarkable multivalence states and the corresponding color evolution.^[87–89] Among the TMOs, vanadium oxide is considered the most promising material for electrochromic displays because of its multicolor behaviors.^[90,91] However, the low electrical conductivity, significant volume expansion during cycling, and the slow reaction kinetics of bulk vanadium oxide prevent its widespread use.^[92,93] In recent years, nanosized vanadium oxides have been studied to mediate these drawbacks because nanostructures provide abundant active sites on the surface and shorten the diffusion paths of ions.^[93] Techniques, such as electrodeposition,^[92] electron beam evaporation,^[94] and the hydrothermal method^[95] were used to synthesize nanosized vanadium oxides. Nonetheless, due to their complicated process and high-energy consumption, these methods hinder the fabrication of large-scale electrodes. Naturally, a solution-processed approach is compatible with large-scale electrode fabrication and high-speed production, thus making

it promising for practical thin film fabrication.^[25,96] Recently, it was reported that the multivalent cations can provide multiple charges to accelerate the redox reactions for fast electrochromic switching times.^[87] A prime candidate for multivalent cations intercalation is vanadium oxides, which so have been utilizing monovalent Li^+ to trigger electrochromism.

Herein, we report a simple, scalable method for synthesizing aqueous V_3O_7 nanoparticle inks that offer the potential for fabricating large-scale thin films via low-cost solution-processed techniques. The Zn-based electrochromic battery system is used to demonstrate a novel electrochromic battery display platform configured with V_3O_7 cathode, Zn anode, and 1 M ZnSO_4 electrolyte. The V_3O_7 cathode delivers a reversible switch between a grayish-blue reduced state and a yellow oxidized state due to the Zn^{2+} insertion (self-coloring/discharging) and extraction (bleaching/charging). This Zn- V_3O_7 electrochromic battery display system, as described, exhibits an optical transmittance contrast of 21% at 632.8 nm, fast self-coloration time of 6.6 s (coloration at 0 V), and rapid switching times of 10.4/28.6 s (coloration at 0.2 V/bleaching at 1.6 V). In addition, we investigate the energy retrieval function of the Zn- V_3O_7 electrochromic display. The Zn- V_3O_7 electrochromic display eliminates the external voltage requirement for the coloration process and retrieves 15.2 mWh g^{-1} (32.6 mWh m^{-2}) from the energy consumed for the bleaching process. For a proof of concept, a prototype aqueous Zn- V_3O_7 electrochromic battery display is constructed by sandwiching a Zn anode between two V_3O_7 cathodes. The prototype display possesses an open circuit potential (OCP) of 1.38 V, which enables the self-coloration behavior and the energy retrieval functionality. Furthermore, the prototype display reversibly switches between the multi-colors (fully yellow, fully grayish-blue, and half

yellow-half grayish-blue images). Such a capability makes the Zn-V₃O₇ electrochromic battery a promising candidate for energy-efficient displays.

4.2 Experimental Section

Materials

All the chemicals were of analytical grade and were used without further purification. Zinc sulfate heptahydrate (ZnSO₄·7H₂O, 99%), zinc foil (Zn, 99.9%), poly(ethyleneimine) solution (PEI, 50% (w/v) in H₂O), vanadium oxychloride (99%), toluene (anhydrous, 99.8%), methanol (anhydrous, 99.8%), and oleylamine (technical grade, 70%) were purchased from Sigma-Aldrich. 1-Octadecanol (97%) is purchased from Alfa Aesar.

Synthesis of Aqueous Vanadium Oxide Ink

The previously reported rapid and scalable method was adopted for the synthesis of V₃O₇ nanoparticle ink.^[97] Briefly, 1-Octadecanol (15.84 g) and oleylamine (60 mL) were added to a 250 mL three-neck flask and degassed under stirring at 125 °C for 1 h. Then, 0.8 mL of vanadium oxychloride was added into the mixtures and heated to 250 °C in an ambient air environment. The temperature was maintained for 30 minutes. Next, purification is conducted by adding toluene and methanol followed by centrifugation for six times. Afterward, the as-synthesized product was thoroughly washed with deionized (DI) water and dispersed in DI water to form a precursor solution (0.5 mg mL⁻¹). The precursor solution was then sonicated in an ultrasonic bath until a clear ink was formed.

Solution-process Fabrication of Electrodes

In order to obtain the accurate mass loading of the V₃O₇ on the ITO-coated glass, the drop-casting method was chosen for the fabrication of electrodes. Prior to drop-casting, the ITO-

coated glass was surface modified by immersing the substrate into 1 wt% PEI solution and DI water for 30 minutes and 5 minutes, respectively. Next, 1.2 mL of V_3O_7 ink was drop-casted onto ITO glass covering an $8\text{ mm} \times 35\text{ mm}$ area. The concentrations of the V_3O_7 colloid used for drop-casting was 0.5 mg mL^{-1} . The V_3O_7 electrodes for the prototype display device were prepared by drop-casting 1.2 mL of V_3O_7 colloid (0.5 mg mL^{-1}) onto a mask (half maple leaf with an area of 2.65 cm^2) covered ITO glass substrate ($5\text{ cm} \times 6\text{ cm}$). All the drop-casted samples were post-annealed in air at $90\text{ }^\circ\text{C}$ for 24 hours.

Characterization

To analyze the composition and structure of samples, X-ray powder diffraction (XRD) (Bruker D8-Advance) with Cu $K\alpha$ -radiation, X-ray photoelectron spectroscopy (XPS) (Kratos AXIS Ultra), transmission electron microscope (TEM) (JEM-ARM200CF, JEOL), and field emission scanning electron microscopy (FE-SEM) (Zeiss SIGMA FESEM, Germany) were used. Binding energy values of the XPS results were corrected to the C 1S peak at 284.6 eV . Electrochemical measurements were carried out using a Zahner electrochemical workstation (Zennium CIMPS-1). A two-electrode configuration was used for electrochemical measurements with Zn foil as the counter electrode in a 1 M ZnSO_4 solution. The self-coloring processes were tested by applying 0 V for 100 s between Zn foil and the V_3O_7 cathode. For the comparison of Li^+ ions and Zn^{2+} ions, a three-electrode configuration was used for electrochemical measurements with Pt wire and Ag/AgCl as counter and reference electrodes in a 1 M ZnSO_4 solution. An Ocean Optics USB4000 spectrometer was used to measure the optical wavelength transmission. No background correction (subtracting the transmittance loss of the ITO-coated glass) was applied to the spectra. The dynamic characterization of the V_3O_7 electrode was conducted by transmitting

632.8 nm laser beam radiation from a helium neon laser. The voltage was applied from Zahner and the photodiode output signal was measured and collected with an oscilloscope. The response times are calculated based on the 90% transmittance change of total optical contrast. The prototype aqueous $\text{Zn-V}_3\text{O}_7$ electrochromic battery display is constructed by sandwiching a Zn anode between two pieces of V_3O_7 cathodes, using the 1 M ZnSO_4 as the electrolyte.

4.3 Results and Discussion

A photograph of the aqueous vanadium oxide ink (0.5 mg mL^{-1}), shown in Figure 4-1a, reveals the high quality of the as-synthesized ink. The green colored colloidal suspension is transparent to the naked eye, while a strong Tyndall effect was observed. This indicates the nanoscale size of the colloidal suspension. To analyze the structure of the as-synthesized ink, the phase composition of the colloidal suspension was dried at room temperature and characterized by powder X-ray diffraction (XRD) measurement. As shown in Figure 4-1b, the diffraction peaks of vanadium oxide nanoparticles can be indexed to the orthorhombic $\text{V}_3\text{O}_7 \cdot \text{H}_2\text{O}$ (JCPDS No. 00-028-1433) phase. The broaden diffraction peaks indicate the small primary particle size and weak crystallinity of $\text{V}_3\text{O}_7 \cdot \text{H}_2\text{O}$. Oxygen deficiency is consistent with the green color of the ink, which is attributed to the presence of V^{4+} (see the original V 2p XPS spectrum of the V_3O_7 film shown in Figure 4-3c). Figure 4-1c and 4-1d show the field emission scanning electron microscopy (FESEM) images of the drop-casted V_3O_7 films, depicting a uniform nanoparticle morphology. The transmission electron microscope (TEM) image, depicted in Figure 4-1e, confirms that the nanoparticle size of the V_3O_7 is approximately 200 nm. Furthermore, as shown in Figure 4-1f, the elemental

mapping images demonstrate the co-existence of O and V elements, which further confirms that the nanoparticle is composed of vanadium oxide.

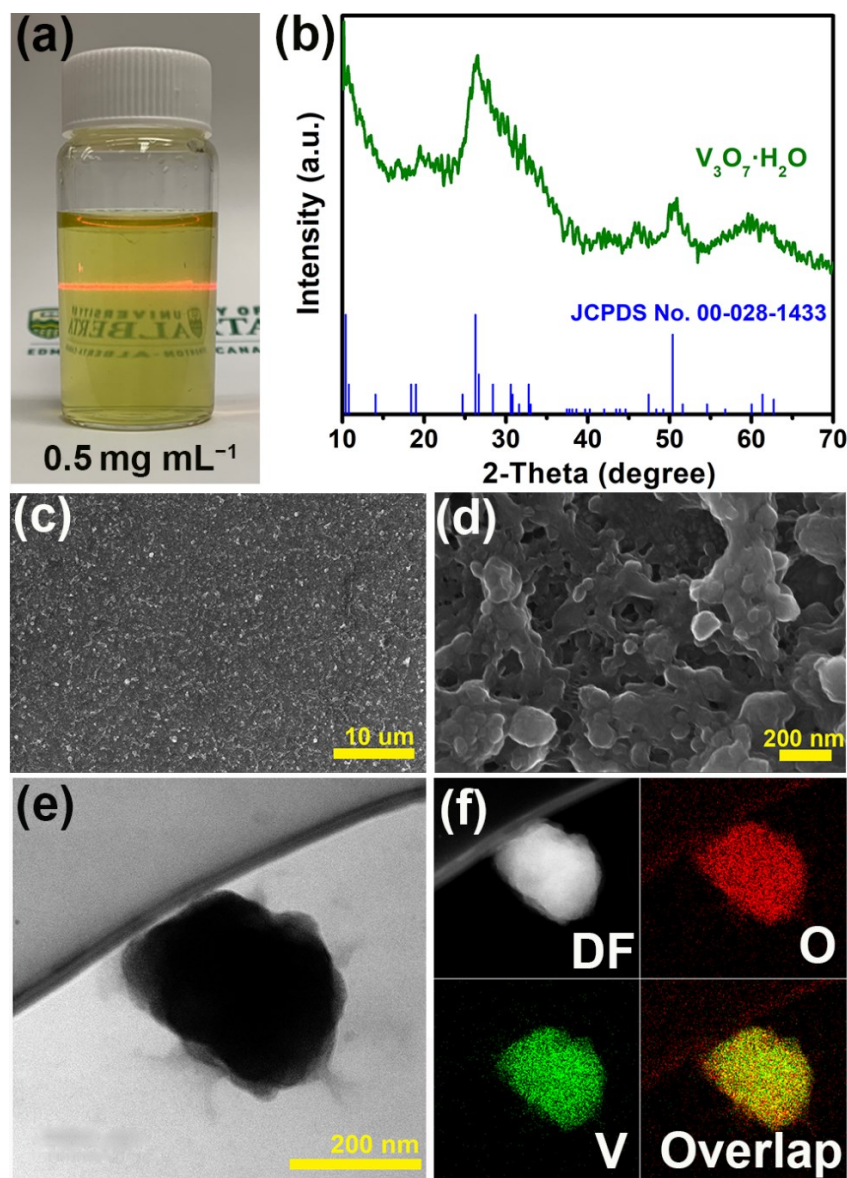


Figure 4-1. (a) Photograph of the V_3O_7 colloidal, the Tyndall effect (632.8 nm laser light scattering) confirms the formation of nanosized suspension. (b) XRD pattern of the green colloidal suspension indicating the formation of small primary particle size and weak crystallinity of $V_3O_7 \cdot H_2O$. (c,d) FESEM images of the prepared V_3O_7 nanoparticle films at low magnification and at high magnification. (e) BF (Bright-field) TEM image of V_3O_7 nanoparticle dropped on TEM grid. (f) DF (Dark-field) TEM image of V_3O_7 nanoparticle and the corresponding elemental mapping images of O, V and the overlapped images.

Notably, since it may be argued that the large radius of hydrated Zn^{2+} would diminish the electrochemical performance of the electrode materials, compared to the small radius of hydrated Li^+ ,^[98] we compared the electrochemical performance of the V_3O_7 electrode via the cyclic voltammetry (CV) scanning in different electrolytes (1 M LiCl and 1 M ZnSO_4 , Figure B-1). Clearly, the utilization of Zn^{2+} significantly enhance the electrochemical performance which is attributed to the small size of the V_3O_7 nanoparticles and the large interlayer space and voids that are accessible for the hydrated Zn^{2+} .^[98] Based on the fact that Zn^{2+} significantly enhances the electrochemical performance of the V_3O_7 film, we assembled an aqueous Zn- V_3O_7 electrochromic battery display (depicted in Figure 4-2a). Here, a zinc foil and a V_3O_7 film were used as the anode and the cathode, respectively, and a 1 M ZnSO_4 solution was used as the electrolyte due to the high electrochemical activity of the V_3O_7 film towards Zn^{2+} . The CV curve of the V_3O_7 nanoparticle film in a two-electrode configuration is depicted in Figure 4-2b. There are two pairs of redox peaks, around 0.49/0.72 and 0.84/1.15 V, indicating a two-step reaction associated with Zn^{2+} ions insertion and extraction through the V_3O_7 electrode. Notably, similar redox peaks were observed in $\text{V}_2\text{O}_5 \cdot n\text{H}_2\text{O}$ for zinc ion batteries.^[99] To understand the electrochemical behavior of this electrode, the galvanostatic charge/discharge processes were measured under different current densities. As depicted in Figure 4-2c, the specific capacities vary from 145 to 67 mAh g⁻¹ as the current densities vary from 100 to 1000 mA g⁻¹. The V_3O_7 electrode delivers an initial discharge capacity of 145 mAh g⁻¹ at 100 mA g⁻¹, with a coulombic efficiency of 87% and round-trip energy efficiency (RTEE) of 93%. The RTEE is an important metric to evaluate the energy retrieval capability of the Zn- V_3O_7 electrochromic battery displays. The high RTEE reveals that 93% of the consumed energy

can be retrieved at a current density of 100 mA g^{-1} . Figure 4-2d shows the change in optical transmittance of the V_3O_7 cathode under different voltages. Notably, the coloration process is a discharging process and the bleaching process is a charging process. During the discharging process (0.2 V), the intercalation of the Zn^{2+} ions into the V_3O_7 cathode triggers a coloration process (grayish-blue). Upon the charging process (1.6 V), the deintercalation of the Zn^{2+} ions induce a bleaching process (yellow). The reversible charging/discharging of V_3O_7 electrode exhibits an optical contrast of 21% at 632.8 nm (without subtracting the transmittance loss of the ITO-coated glass). In Figure 4-2e, the in situ self-coloring time (Zn^{2+} ions insertion) of the V_3O_7 cathode is measured at 0 V for 100 seconds. The self-coloration time, defined as the time required for achieving 90% of maximum optical contrast,^[100] is measured to be 6.6 seconds. This self-coloration time is faster than the previously reported coloration time ($\sim 18 \text{ s}$) of vanadium oxide nanowire films triggered by external voltages.^[101] The V_3O_7 electrode shows fully discharged capacity and charged capacity at 0.2 V and 1.6 V, respectively (Figure 4-2c). This indicates the V_3O_7 electrode can be fully colored under 0.2 V and bleached under 1.6 V. Thus, the dynamic transmittance characterization of the V_3O_7 electrode was tested in the 0.2-1.6V window. As shown in Figure 4-2f, the response times are calculated to be 10.4 seconds for coloration and 28.6 seconds for bleaching. Moreover, the coloration efficiency (CE), defined as the change in optical density (ΔOD) per unit of charge intercalated into the electrochromic layer,^[79] is measured to be $20.6 \text{ cm}^2 \text{ C}^{-1}$ (Figure B-2). The CE value is similar to the value reported for Li^+ -based vanadium oxide electrochromic films,^[92,102] indicating Zn^{2+} ions are efficient and promising in electrochromic battery displays.

To evaluate the energy efficiency of this $\text{Zn-V}_3\text{O}_7$ electrochromic battery display during

rapid switching processes, energy densities of both coloration process and bleaching process during the selected round-trip cycle in Figure 4-2f are compared and shown in Figure 4-2g. As depicted in Figure 4-2g, 15.2 mWh g^{-1} (32.6 mWh m^{-2}) is retrieved from 94.7 mWh g^{-1} (202.9 mWh m^{-2}). This indicates that the round-trip net-energy consumption is only 79.5 mWh g^{-1} (170.3 mWh m^{-2}). Furthermore, it should be noted that the electrochromic battery display has eliminated the energy consumption during the coloration process. There is only one process consuming energy in the electrochromic battery display, while the traditional electrochromic display consumes energy in both coloration and bleaching processes. The low value of the retrieved energy is attributed to the chosen low discharge bias for a rapid coloration process (i.e. there is an interplay between the fast switching time requirement and high energy retrieval capability). The amount of retrieved energy can be further improved via the design of high-conductive electrode materials having open-framework structures.^[103] The cycle stability of the drop-casted film is shown in Figure B-3, which requires a further study on the interface engineering to improve the cycle performance.^[30]

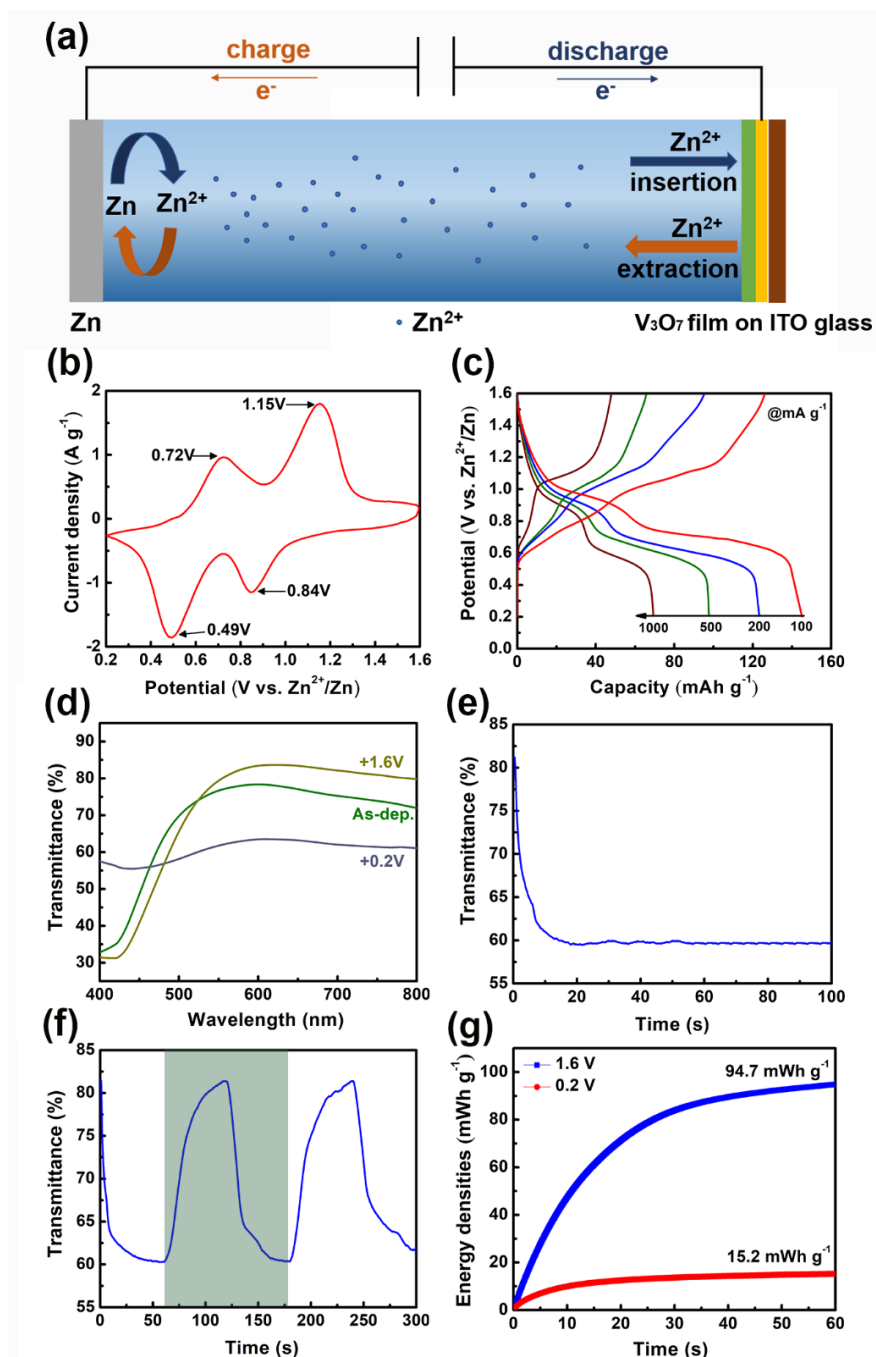


Figure 4-2. (a) Schematic illustration of an aqueous Zn/V₃O₇ cell. (b) CV curve of V₃O₇ film tested via a two-electrode configuration in 1 M ZnSO₄ solution. (c) Charge-discharge curves of V₃O₇ film at various current densities. The pair of curves in the same color refers to the charge and the discharge processes, respectively. (d) Optical transmittance of the V₃O₇ electrode under different voltages for 100 s: green initial state (As-dep.), grayish-blue reduced state (0.2 V) and yellow oxidized state (1.6 V). (e) In situ self-coloring (discharge) process of the V₃O₇ electrode. (f) In-situ transmittance spectrum of the V₃O₇ electrode at 632.8 nm under pulsed voltages of 0.2 V (coloring) for 60 s and 1.6 V (bleaching) for 60 s. (g) Energy densities comparison during the selected round-trip cycle in Figure 4-2f.

To shed light on the operation of the Zn-V₃O₇ electrochromic battery display, X-ray photoelectron spectroscopy (XPS) was carried out to evaluate the valence state of the V accompanied by Zn²⁺ ions insertion/extraction. As illustrated in Figure 4-3a, the XPS survey spectrum of the as-deposited V₃O₇ film indicates the presence of only V and O elements, without other impurities. After coloration under 0.2 V, the presence of Zn confirms the insertion of Zn²⁺ ions. After being bleached under 1.6 V, the weak intensities of Zn 2p peaks indicate that most of the Zn²⁺ ions are extracted from the V₃O₇ electrode. The presence of Zn²⁺ residue in the electrode is due to the intercalated Zn²⁺ ions are trapped at the “dead Zn²⁺ sites” and cannot be extracted from the V₃O₇ lattice during the following bleaching process.^[104] Nonetheless, the trapped Zn²⁺ ions can be extracted from the dead Zn²⁺ sites by applying a high current.^[105] These findings are further confirmed by the high resolution Zn 2p core level XPS spectra (Figure 4-3b). As expected, the intercalation/deintercalation of Zn²⁺ ions would induce the valence state change of the V. Figure 4-3c depicts the high-resolution V 2p core level XPS spectra of the V₃O₇ film under different states. The most intense doublet peaks are located at 517.6 and 524.8 eV. These peaks are assigned to the V⁵⁺ ions.^[106] Another pair of peaks, centered at 516.2 and 523.0 eV, are assigned to the V⁴⁺ ions. The atomic ratio of V⁵⁺/V⁴⁺ for the as-deposited V₃O₇ film is estimated to be 2.13 (Table B-1), which is approximately equal to the atomic ratio of V⁵⁺ and V⁴⁺ ions in the V₃O₇.^[107] During the coloration process (0.2 V), the high valence state of V⁵⁺ was partially reduced to V⁴⁺ and the atomic ratio of V⁵⁺/V⁴⁺ decreased to 0.32 (Table B-1). Interestingly, the V⁵⁺/V⁴⁺ atomic ratio of the bleached film (1.6 V) is estimated to be 4.88 (Table B-1), which is larger than the ratio of the as-deposited V₃O₇ film. The larger V⁵⁺/V⁴⁺ ratio induces a high transmittance of the electrode, as confirmed in the

transmittance spectra shown in Figure 4-2d.

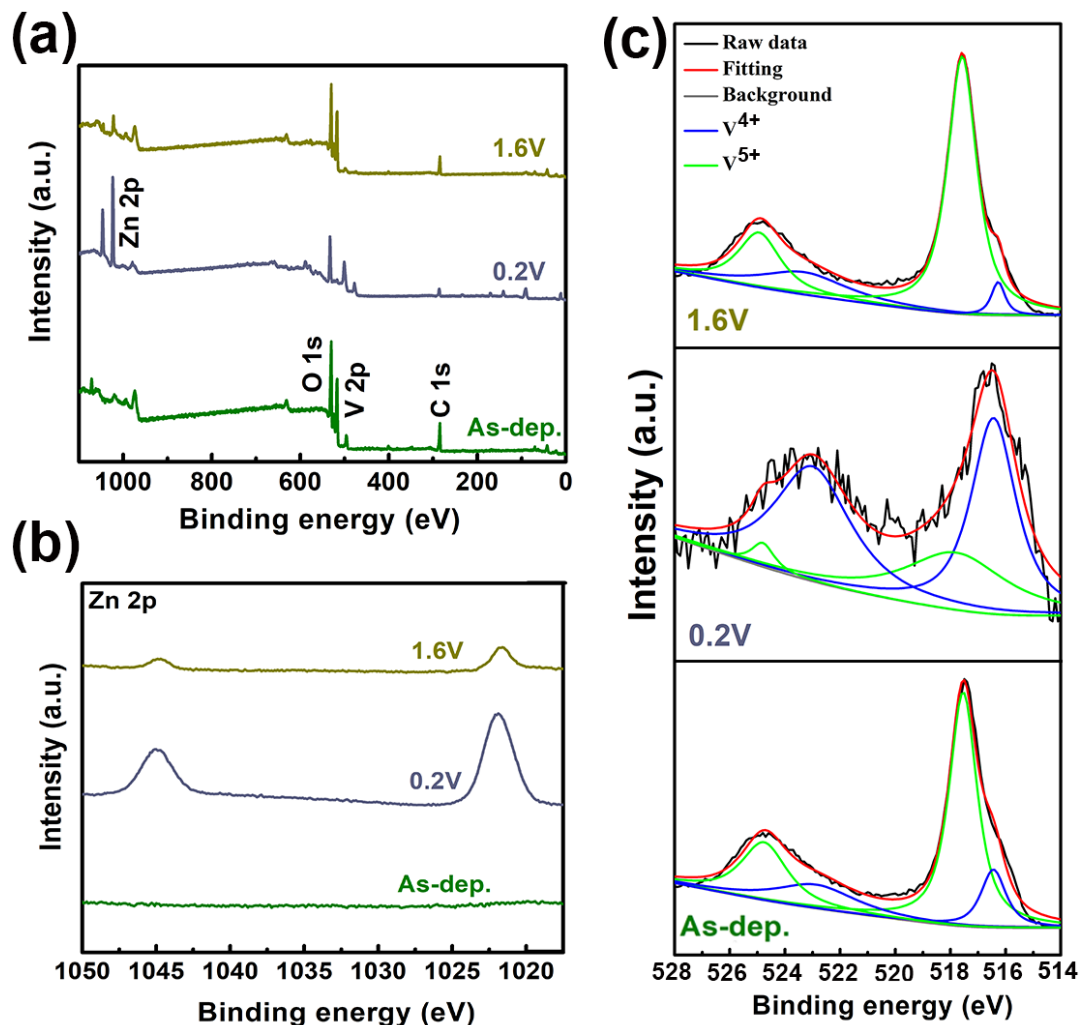


Figure 4-3. (a) XPS survey spectrum of the V_3O_7 film during discharging/charging. (b) Zn 2p XPS spectrum of the V_3O_7 film during discharging/charging. (c) V 2p XPS spectrum of the V_3O_7 film during discharging/charging.

To further evaluate the performance of the vanadium oxide electrodes for practical use in electrochromic battery displays, a prototype $5\text{cm} \times 6\text{cm}$ device was assembled as shown schematically in Figure 4-4a. The V_3O_7 films were prepared on an ITO-coated glass substrate (formed into a half maple leaf shape) by a drop-casting technique. The combination of the two pieces of V_3O_7 electrode form a complementary full maple leaf.

The demonstrated electrochromic battery display, showing the pattern of a yellow maple leaf (oxidized state), has an open circuit potential (OCP) of 1.38 V (Figure 4-4b). Despite the fact that the standard electrode potential of Al anode being higher than Zn anode, the OCP value is slightly higher than the value of previously reported Al^{3+} -based electrochromic battery,^[108] Figure 4-4c depicts the functionalities of the electrochromic battery display captured in digital images. The reversible switching of multicolor displays (fully yellow, fully grayish-blue and half yellow-half grayish-blue maple leaves) are operated either via lighting an 0.5 V regulated LED for self-coloring process (grayish-blue) or through applying an external voltage of 1.6 V for bleaching process (yellow). The LED can be powered for more than 28 min (Figure 4-4d and 4-4e), indicating the good energy retrieval capabilities of the electrochromic battery display prototype. The dynamic transmittance characterization of the electrochromic battery display at an optical wavelength of 632.8 nm is evaluated by applying the pulsed voltages of 0.2 (60 s) and 1.6 V (60 s) (Figure 4-4f). Remarkably, the reversible coloring/bleaching processes of the electrochromic battery display exhibits an optical contrast of 19 % at 632.8 nm. The response times, similar to the performance of the single V_3O_7 cathode (Figure 4-2f), are calculated to be 12 s for coloration and 30.4 s for bleaching, respectively. Furthermore, the energy densities comparison during the dynamic switch between colored state and bleached state are shown in Figure 4-4g. Here, 14.4 mWh g^{-1} (32.6 mWh m^{-2}) is retrieved from 88.9 mWh g^{-1} (201.2 mWh m^{-2}). Even though the response times and the retrieved energy show a slight decay compared to the Zn- V_3O_7 system tested in a cuvette, the demonstrated electrochromic battery display is a promising technology for large-scale and energy-efficient electrochromic displays.

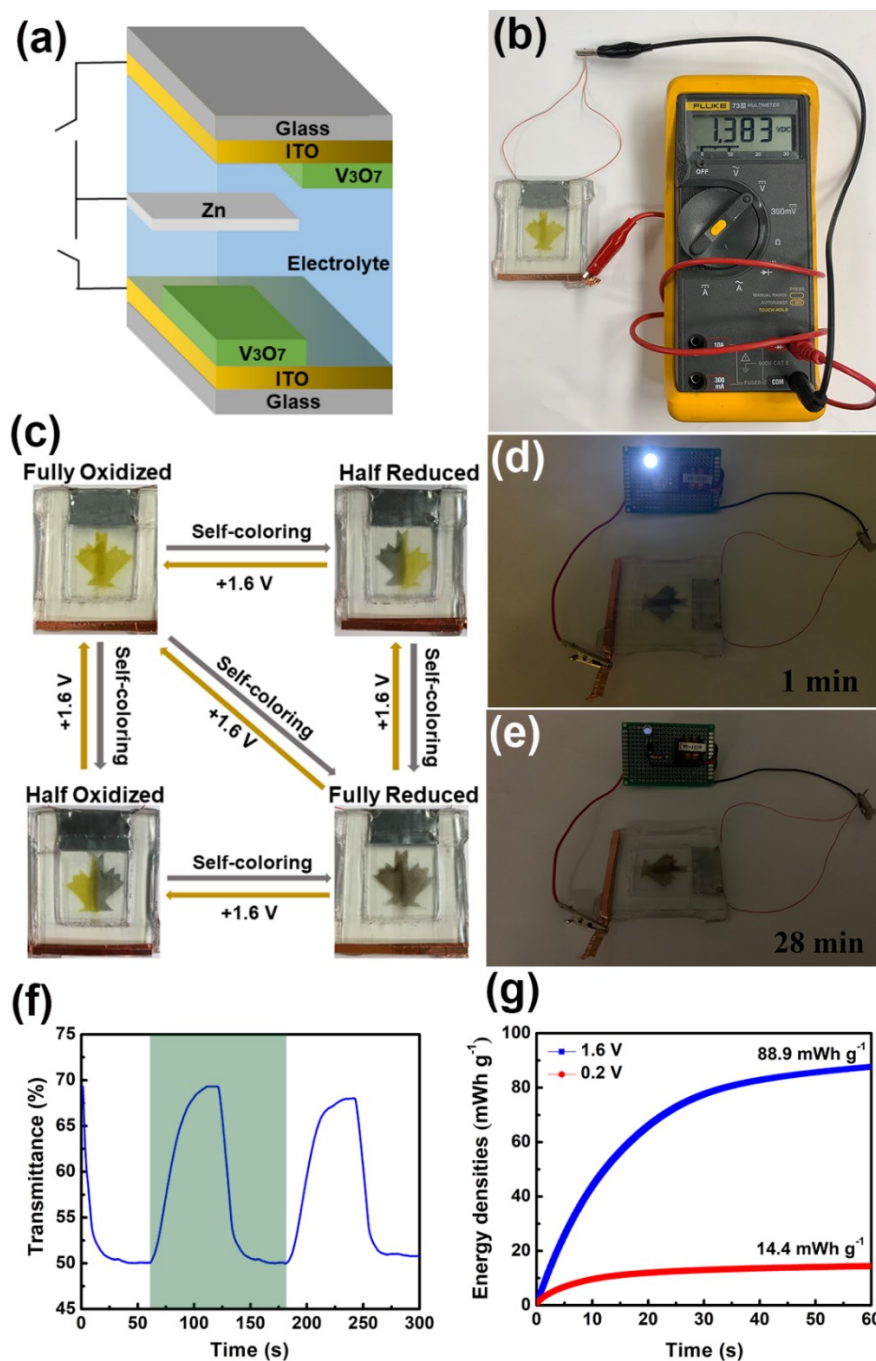


Figure 4-4. (a) Schematic illustration of the prototype electrochromic battery display. (b) Digital photograph of the electrochromic battery display, showing the pattern of a yellow maple. The OCP of 1.38 V indicates the electrochromic battery display is under a charged state. (c) The functionalities of the demonstrated electrochromic battery display with digital photographs. (d,e) The digital photographs of a 0.5 V regulated LED powered by electrochromic battery display at 1 and 28 min. (f) In-situ transmittance spectrum of the electrochromic battery display by applying pulsed voltages of 0.2 (60 s) and 1.6 V (60 s) at an optical wavelength of 632.8 nm. (g) Energy densities comparison during the selected round-trip cycle in Figure 4-4f.

4.4 Summary

A simple, scalable method for synthesizing aqueous V_3O_7 nanoparticle inks was reported, which offers the potential for fabricating large-scale thin films via solution-processed techniques. Using drop-casted V_3O_7 electrodes as cathodes and Zn foils as anodes, the process was used to realize novel Zn- V_3O_7 electrochromic battery displays. The V_3O_7 cathode delivers a reversible switch between a grayish-blue reduced state and a yellow oxidized state associated with Zn^{2+} ions insertion (self-coloring/discharging) and extraction (bleaching/charging). This Zn- V_3O_7 electrochromic battery display platform exhibits an optical transmittance contrast of 21% at 632.8 nm, high self-coloration time of 6.6 seconds (coloration at 0 V) and rapid switching times of 10.4/28.6 seconds (coloration at 0.2 V/bleaching at 1.6 V). Moreover, for the first time, we demonstrated energy retrieval function of an electrochromic display. It was found that 15.2 mWh g^{-1} (32.6 mWh m^{-2}) of energy can be recovered back. As a proof of concept, a prototype aqueous Zn- V_3O_7 electrochromic battery display was constructed and showed the display can reversibly switch between the multi-colors (fully yellow, fully grayish-blue and half yellow-half grayish-blue maple leaves), along with the energy retrieval function via lighting an LED for 28 min. These findings present a new paradigm in synthesizing aqueous V_3O_7 nanoparticle inks for electrochromic battery display having energy retrieval capability, as such facilitating the development of energy-efficient electrochromic displays.

Chapter 5

Conclusion and Future Outlook

5.1 Conclusion

This thesis presented recent efforts in developing energy-efficient smart windows. We demonstrate that MoO_{2+x} films, where Mo in the valence state of IV and V, can be used for high-performance supercapacitor electrodes. As the counter electrode, the introduction of MoO_{2+x} counter electrode remarkably lowers the activation and bleaching potential of WO_3 electrochromic layer. These properties make the MoO_{2+x} film an ideal counter electrode to store ions for an electrochromic supercapacitor. To put this MoO_{2+x} based smart window into perspective within the state-of-the-art smart window platforms, Table 5-1 summarizes and compares the key electrochromic metrics. Clearly, this MoO_{2+x} based smart window exhibits a high optical contrast and rapid switching times.

Table 5-1. Comparison of current state-of-the-art smart windows.

Ref.	Device	Coloration	Bleaching	ΔT	Response time (s)	State of electrolyte	Size (cm^2)
This work	$\text{WO}_3 \text{MoO}_{2+x}$	-0.5 V	0.5 V	63% at 632.8 nm	Coloration: 24.2 Bleaching: 32	gel	9
Cheng et al. ¹⁰⁹	$\text{WO}_3 \text{FTO}$	-3.5 V	3 V	~65% at 700 nm	Coloration: 17 Bleaching: 15	liquid	100
Wang et al. ¹¹⁰	$\text{WO}_3 \text{FTO}$	-1 V	1 V	~60% at 700 nm	—	gel	9
Azam et al. ¹¹¹	$\text{WO}_3 \text{ITO}$	-3 V	3 V	~63% at 700 nm	Coloration: 10.7 Bleaching: 6.9	liquid	—
Li et al. ³⁰	$\text{MoO}_3\text{-W}_{0.71}\text{Mo}_{0.29}\text{O}_3 \text{NiO}$	-2.5 V	2.5 V	~41.9 % at 632.8 nm	—	liquid	64

Cai et al. ²⁷	WO ₃ CeO ₂	-0.7 V	1 V	~73% at 633 nm	Coloration: 12.7 Bleaching: 15.8	liquid	20.25
Zhang et al. ¹¹²	WO ₃ LiAl	1.6 V	4 V	~77% at 633 nm	Coloration: 19 Bleaching: 71	liquid	4
Zhang et al. ⁸⁷	WO _{3-x} ITO	-4 V	1 V	~73% at 650 nm	—	liquid	~2.8
Cao et al. ⁸⁹	Ta-TiO ₂ NiO	-3.5 V	1 V	~72.7 % at 550 nm	—	liquid	~3.75
Li et al. ⁴⁰	W _{0.71} Mo _{0.29} O ₃ FTO	-3.5 V	1.5 V	~68% at 632.8 nm	—	liquid	100
Zhang et al. ¹¹³	WO _{3-x} ITO	-2.8 V	1.2 V	~71.1 % at 633 nm [@]	Coloration: 30 Bleaching: 17	liquid	~4
Lang et al. ¹¹⁴	ECP-Magenta MC CP	-0.5 V	0.8 V	~38% at 550 nm	Coloration: 5.7 Bleaching: 19	gel	10

Interestingly, MoO_{3-y} films, where Mo in the valence state of V and VI, exhibit excellent catalytic properties for hydrogen evolution reaction (HER). Furthermore, we show that MoO₃ films, where Mo is at its highest oxidation state (VI), exhibit battery characteristics. This strategy to fabricate sub-stoichiometric molybdenum oxide nanofilms with supercapacitive properties lowers the activation and bleaching potential of the electrochromic layers and further lowers the energy consumption of smart windows. Moreover, the effect of different valences (IV, V and VI) on the electrochemical performance of the molybdenum oxide films was revealed, which has the potential to be applied to other transition metal oxides.

Next, a scalable method to synthesize an aqueous V₃O₇ nanoparticle ink is presented, which is compatible with solution-process techniques for aqueous Zn-V₃O₇ electrochromic battery displays. The newly developed Zn-V₃O₇ electrochromic battery displays eliminate the energy consumption for coloration while retrieving the consumed energy for bleaching. For a proof of concept, a prototype display is constructed. The display prototype can reversibly switch between the multi-colors (fully yellow, fully grayish-blue and half yellow-half grayish-blue images) and partially retrieves the consumed energy. This research presents a

facile strategy to synthesize aqueous V_3O_7 inks, as well as a novel electrochromic battery display having energy retrieval functions, thus facilitating the development of energy-efficient electrochromic devices.

5.2 Future Outlook

The previous work showed that MoO_{2+x} film as the ion storage layer in a complementary electrochromic device can remarkably decrease the activation potential of WO_3 . However, the frame shape of the MoO_{2+x} film limits the diffusion of ions. Changing the electrodeposition electrolyte and other parameters, such as complexing agents and additives, can help to synthesize a thin film that combines supercapacitive properties and high transmittance. Hence, the frame-shaped counter electrode can be replaced by a plane-parallel counter electrode, which maintains constant transverse ion diffusion regardless of scale.

Moreover, electrochromic batteries that incorporate electrochromic phenomena and energy storage functionalities in a single device are promising for green and renewable energy storage applications. The novel electrochromic battery display having energy retrieval functions was presented. Further investigation of electrochromic batteries based on different electrochromic materials may be a promising direction for future research.

Appendices

Appendix A: Characterization of molybdenum oxide films

Schematic of electrodeposition, EIS, SEM, XPS, CV, and stability test of molybdenum oxide films are included.

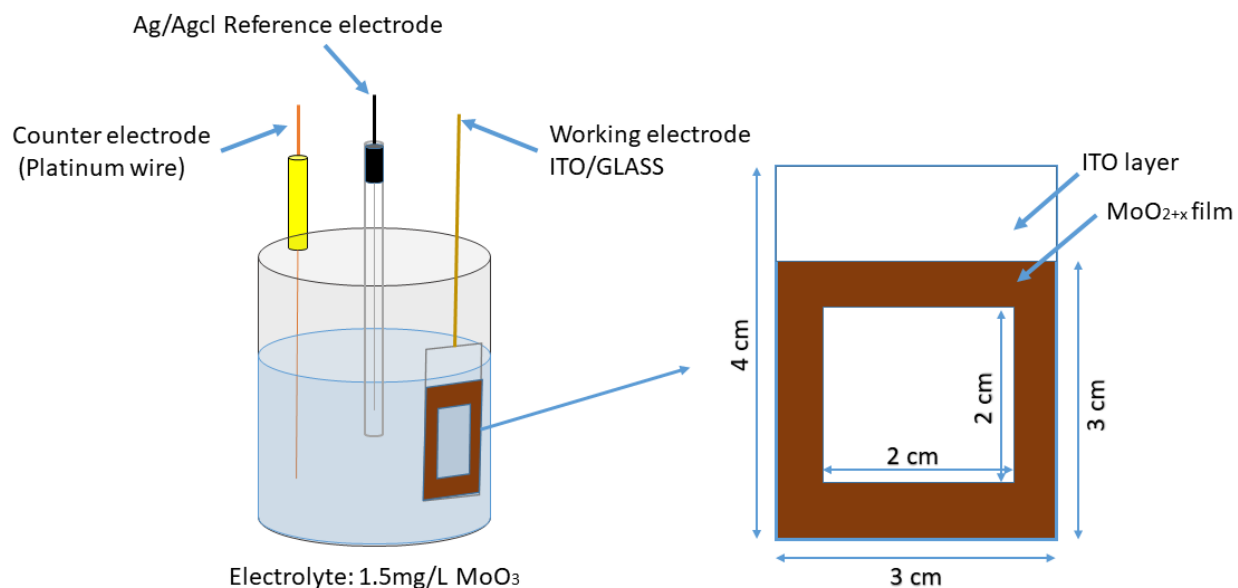


Figure A-1. Schematic of MoO_{2+x} films electrodeposited on ITO glass

A $2 \text{ cm} \times 2 \text{ cm}$ area of the ITO film was removed from the substrate, via laser ablation, to create a non-conductive region on the glass substrate. A three-electrode configuration was used to electrodeposit MoO_{2+x} films, with Pt wire, ITO glass, and Ag/AgCl as the counter, working and reference electrodes, respectively. The MoO_3 colloid was electrodeposited onto an effective $3 \times 3 \text{ cm}^2$ area of the ITO glass substrate at a pulsed (1 second) current of -0.3 mA cm^{-2} and a pulsed (3 seconds) 0.03 mA cm^{-2} for 1,200 cycles, to obtain the MoO_{2+x} film.

Table A-1. Atomic ratio of Mo (IV, V and VI) in MoO_{2+x} , MoO_{3-y} , and MoO_3 films.

Sample	Atomic ratio of Mo			Value of x or y
	Mo (IV)	Mo (V)	Mo (VI)	
MoO_{2+x}	0.61	0.39	-	0.20
MoO_{3-y}	-	0.52	0.48	0.26
MoO_3	-	-	1.00	-

For MoO_{2+x} film, the atomic ratio of Mo (IV) and Mo (V) is estimated to be 1.56, which indicates that the value of x is ~ 0.20 .

For MoO_{3-y} film, the atomic ratio of Mo (V) and Mo (VI) is estimated to be 1.08, which indicates that the value of y is ~ 0.26

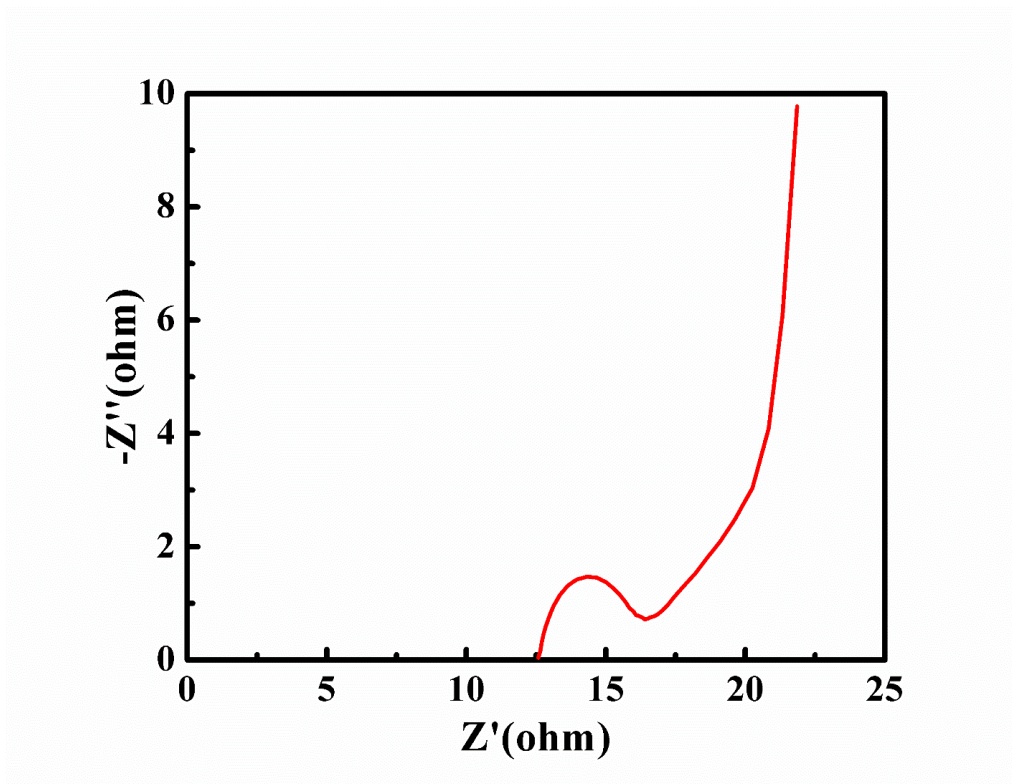


Figure A-2. Electrochemical Impedance Spectroscopy (EIS) of MoO_{2+x} electrode in 0.5M H₂SO₄ solution.

The Nyquist plot of the MoO_{2+x} electrode is composed of semi-circle component at high frequency (HFS) and linear component at low frequency. The small semi-circle component demonstrates a low resistance of H⁺ ions migration through the surface of electrodes. While only one semi-circle is shown in high frequency region, the absence of middle-to-low frequency semicircle (MLFS) contributes to low charge transfer resistance. Also, the plot shows a short Warburg region, indicating fast diffusion of H⁺ ions. At lowest frequency region, the steep line reflects capacitive behavior, confirmed that MoO_{2+x} films are promising for supercapacitors.^[30,68]

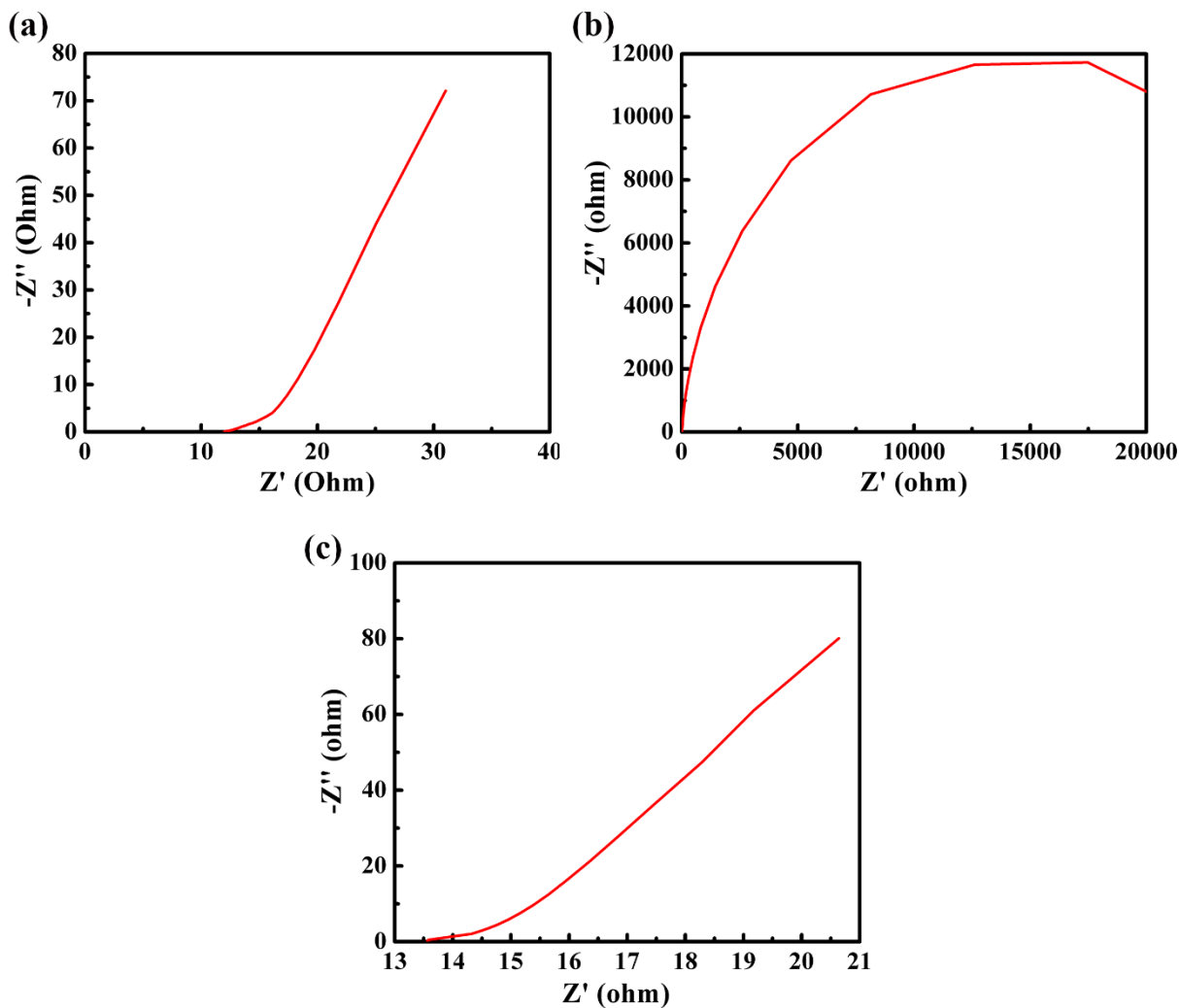


Figure A-3. EIS of (a) MoO_{3-y} electrode and (b) bare ITO substrate (c) magnified high-frequency region of bare ITO glass. All tests were conducted in 0.5M H₂SO₄ solution.

The intercept of the plot on real axis is defined as internal resistance (R_s), which is used for the correction of LSV curve. In Figure A-3a, compared to MoO_{2+x} electrode, while the inclined line, the Nyquist plot of MoO_{3-y} electrode in Warburg region shows a tendency to move toward the real axis, indicating a relatively slow diffusion of H⁺ ions. Bare ITO substrate shows an extremely large middle frequency semicircle in Figure A-3b, which is attributed to poor charge-transfer through the electrode/electrolyte interface.

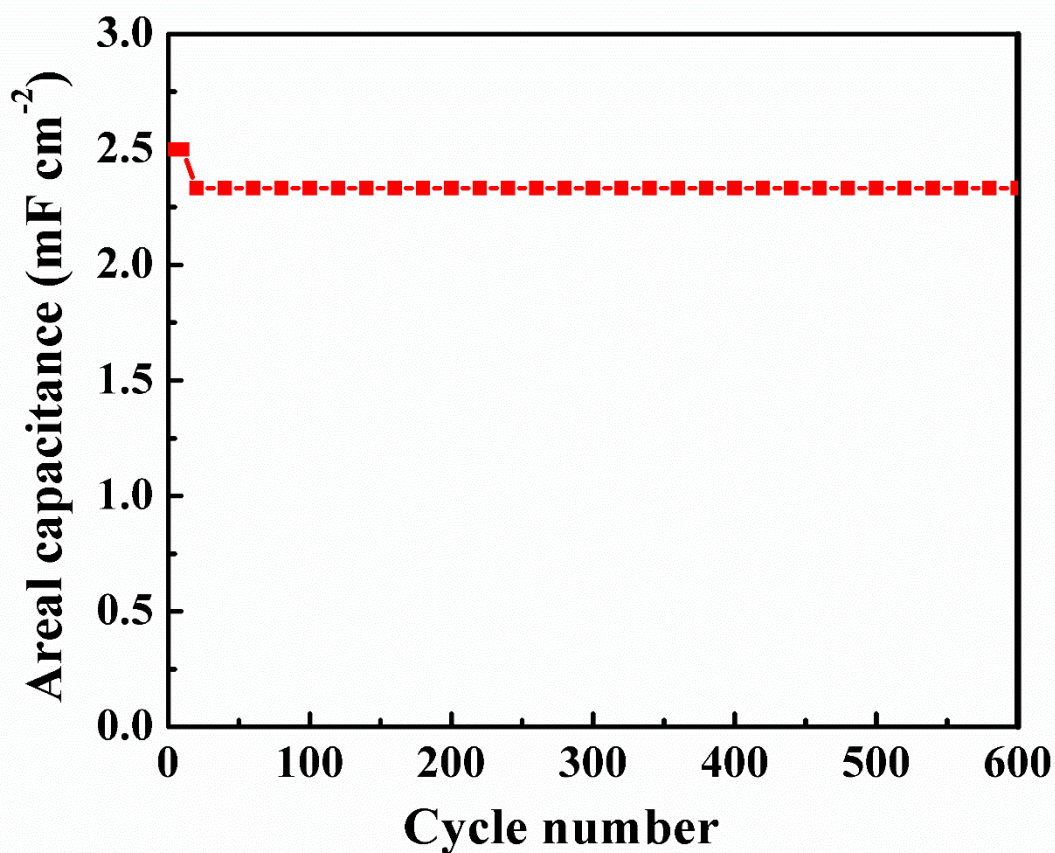


Figure A-4. Cycle performance of MoO_{2+x} nanofilm.

In Figure A-4, only a slight reduction was observed in first 20 cycles for the cycle performance of MoO_{2+x} nanofilm. The reason is that some nanoparticles which are poorly connected to ITO substrate will become detached, thus leading to reduction of areal capacitance in first 20 cycles.^[79] After 20 cycles, capacitance loss is negligible.

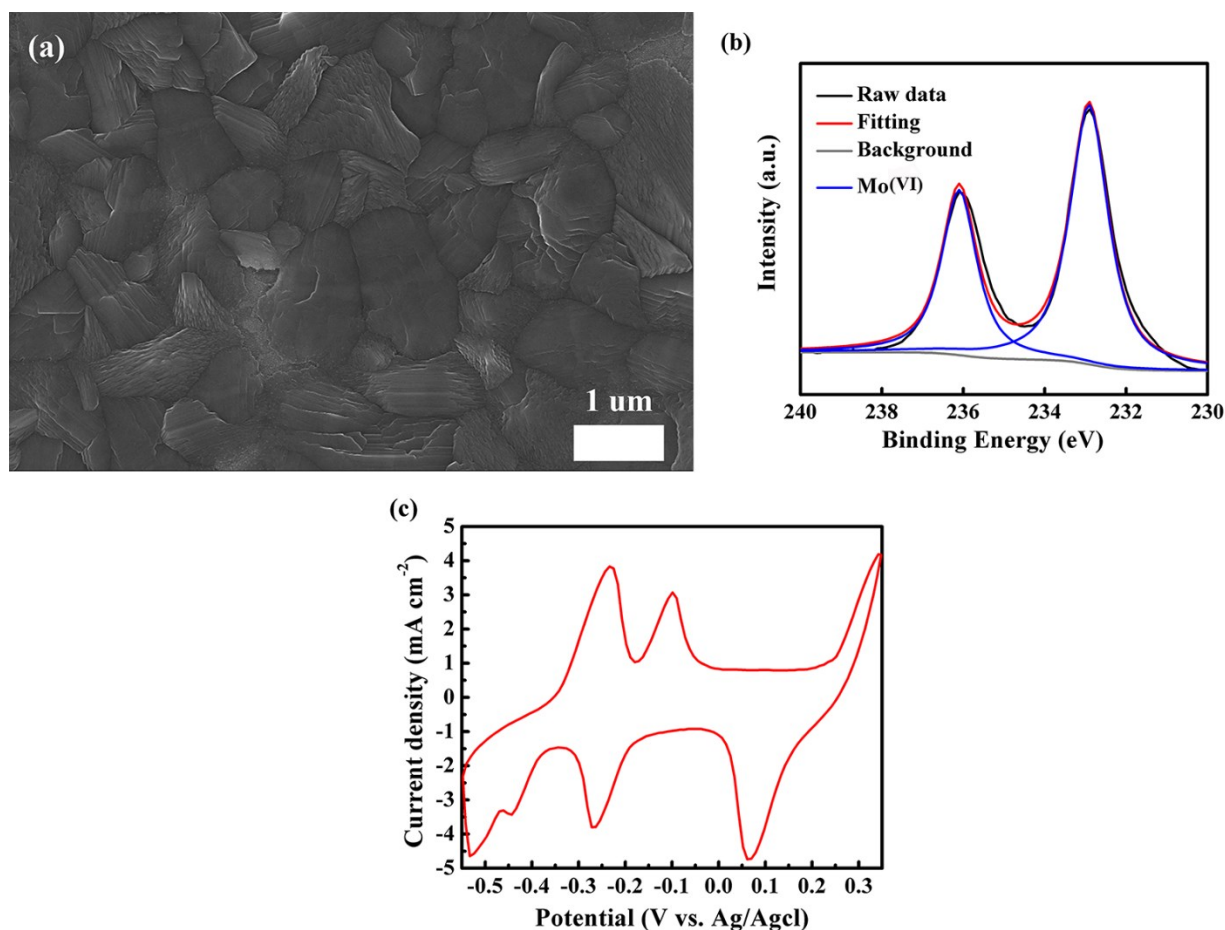


Figure A-5. (a) FESEM image of as prepared MoO₃ nanofilm. (b) Mo 3d XPS spectrum of MoO₃. (c) CV curve for α-MoO₃ in 0.5M H₂SO₄ solution at scan rate of 50mV s⁻¹.

In Figure A-5a, the morphology of MoO₃ films were evaluated by field emission scanning electron microscopy (FESEM), suggesting concentrated nanoflakes structure of α-MoO₃.^[80] In Figure A-5b, the high-resolution XPS Mo 3d core level spectrum shows only Mo (VI) peak which is an indication of a full elimination of oxygen vacancies. Furthermore, the CV curve of α-MoO₃ in Figure A-5c shows clear redox reaction peaks, which suggests that the α-MoO₃ film can be utilized as a battery electrode.

Appendix B: Characterization of vanadium oxide nanoparticle films

Atomic ratio, CE, CV, and stability test of vanadium oxide nanoparticle films are included.

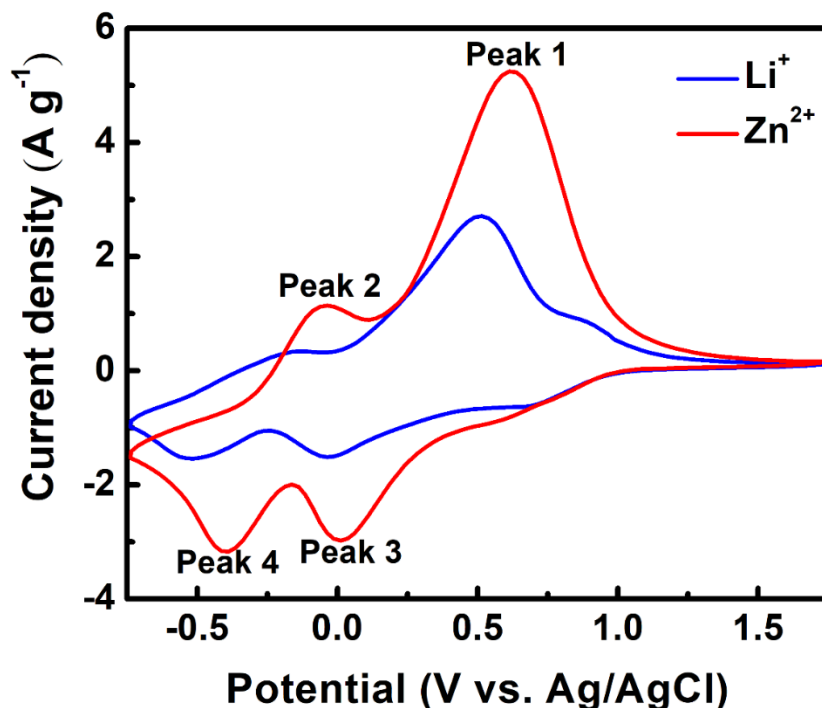


Figure B-1. Cyclic voltammetry (CV) measurement of V_3O_7 electrodes performed at 50 mV s^{-1} scan rate in 1M LiCl electrolyte and 1M $ZnSO_4$ electrolyte.

The CV curves of the V_3O_7 electrodes in different electrolytes (1M LiCl and 1M $ZnSO_4$) are shown in Figure B-1. The two anodic peaks located at 0.61 (Peak 1) and -0.06 V (Peak 2) and two cathodic peaks located at 0.01 (Peak 3) and -0.39 V (Peak 4) suggest a multistep intercalation and deintercalation process. The CV curve of the V_3O_7 cathode, measured in the $ZnSO_4$ electrolyte, exhibits higher current densities (~ 1.9 times higher at Peak 1, ~ 3.3 times higher at Peak 2, ~ 2.0 times high at Peak 3 and ~ 2.1 times high at Peak 4), compared to that tested in LiCl. This indicates that the V_3O_7 cathode is more electrochemically active towards the Zn^{2+} (i.e. attributed to the small size of the V_3O_7 nanoparticles and the large interlayer space and voids that are accessible to the hydrated Zn^{2+}).

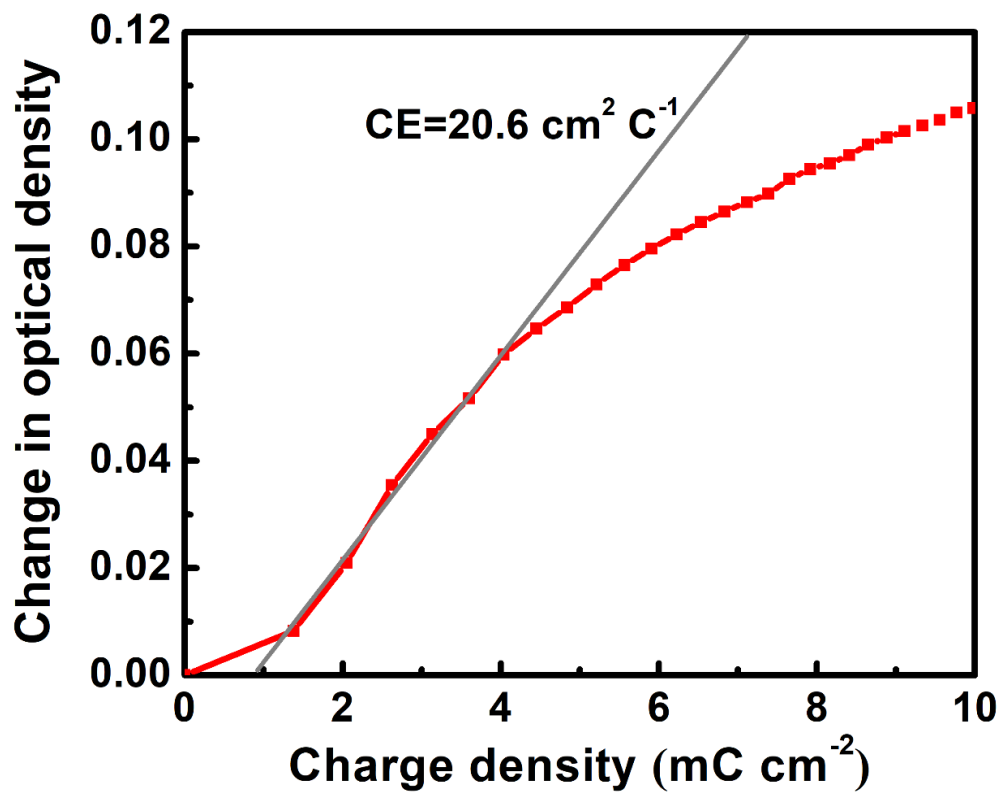


Figure B-2. Coloration Efficiency (CE) of vanadium oxide nanoparticle film.

The coloration efficiency, defined as the change in optical density (ΔOD) per unit of charge intercalated into the electrochromic layer, is measured to be $20.6 \text{ cm}^2 \text{ C}^{-1}$ of vanadium oxide film (Figure B-2). This value is similar to the CE of Li^+ -based vanadium oxide electrochromic films which are triggered by an external potential.^[92,102] The CE value indicates that the Zn^{2+} ions are efficient intercalating ions for electrochromic displays.

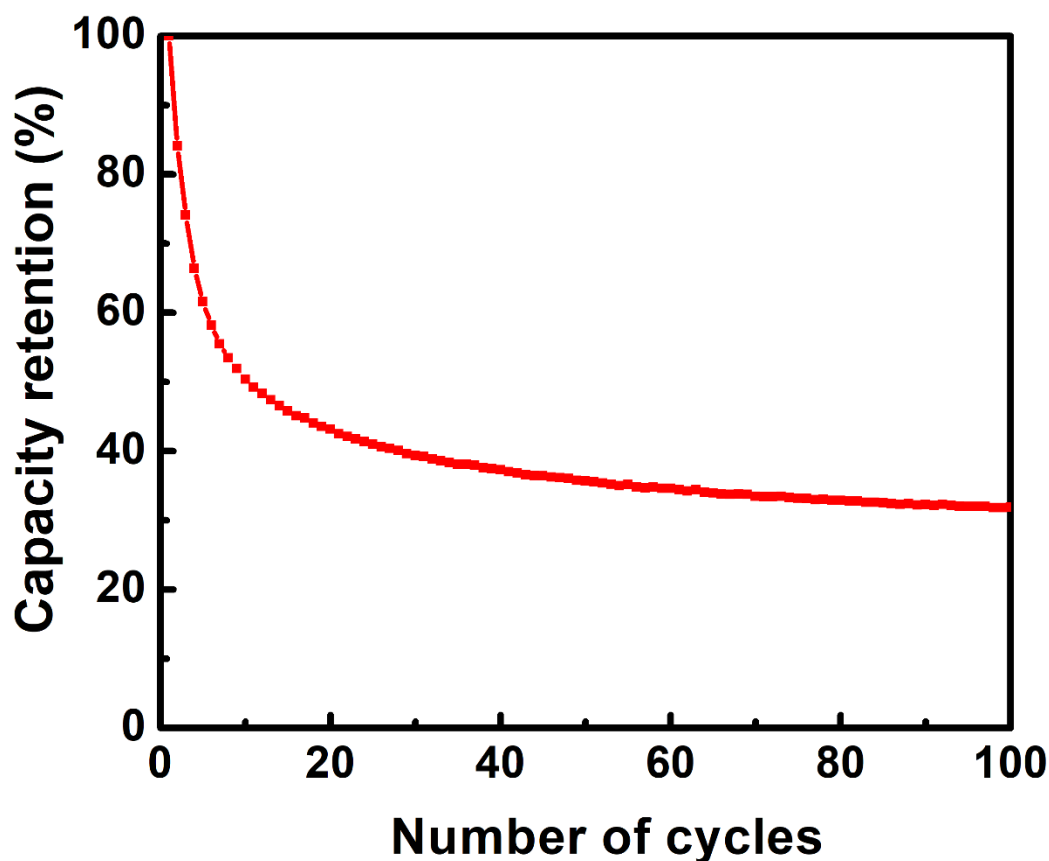


Figure B-3. Cycle performance of the V_3O_7 nanoparticle films at 1000 mAh g^{-1} .

In Figure B-3, there is only 40% capacity retention after 100 cycles because of the limitation of the film deposition technique (drop-casting method). Some of the drop-casted nanoparticles are poorly adhere to the ITO substrate and detach during the charging/discharging processes. A further study on the interface engineering to improve the cycle performance is a necessary. Clearly, the synthesized high-quality ink requires a better methodology for film fabrication.

Table B-1. Atomic ratio of V^{4+} and V^{5+} in the as-deposited, reduced and oxidized vanadium oxide films.

Sample	Atomic percentage of V in different valence states		V^{5+}/V^{4+}
	V^{5+}	V^{4+}	
As-deposited	0.68	0.32	2.13
Reduced (0.2 V)	0.24	0.76	0.32
Oxidized (1.6 V)	0.83	0.17	4.88

For the as-deposited vanadium oxide film, the atomic ratio of V^{5+}/V^{4+} is estimated to be 2.13 (Table B-1), which is approximately equal to the atomic ratio of V^{5+} and V^{4+} ions in crystalline V_3O_7 .^[107] With the decrease/increase of the atomic ratio of V^{5+}/V^{4+} during discharging/charging, the V_3O_7 films switch reversibly between a grayish-blue reduced state (0.2 V) and a yellow oxidized state (1.6 V) associated with Zn^{2+} ions insertion and extraction.

References

- (1) *Survey of Commercial and Institutional Energy Use, 2014*. Statistics Canada **2016**.
- (2) Ou, J. Z.; Balendhran, S.; Field, M. R.; McCulloch, D. G.; Zoolfakar, A. S.; Rani, R. A.; Zhuikov, S.; O'Mullane, A. P.; Kalantar-Zadeh, K. The Anodized Crystalline WO₃ Nanoporous Network with Enhanced Electrochromic Properties. *Nanoscale* **2012**, 4, 5980–5988.
- (3) Cai, G.; Cui, M.; Kumar, V.; Darmawan, P.; Wang, J.; Wang, X.; Lee-Sie Eh, A.; Qian, K.; Lee, P. S. Ultra-Large Optical Modulation of Electrochromic Porous WO₃ film and the Local Monitoring of Redox Activity. *Chem. Sci.* **2016**, 7, 1373–1382.
- (4) Korgel, B. a. Materials Science: Composite for Smarter Windows. *Nature* **2013**, 500, 278–279.
- (5) Platt, J. R. Electrochromism, a Possible Change of Color Producing in Dyes by an Electric Field. *J. Chem. Phys.* **1961**, 34, 862–863.
- (6) Deb, S. K. A Novel Electrophotographic System. *Appl. Opt. Suppl.* **1969**, 8, 192–195.
- (7) Risser, R. *Making Smart Windows Smarter*. U.S. Department of Energy **2011**.
- (8) Lee, E. S.; Yazdani, M.; Selkowitz, S. E. *The Energy-Savings Potential of Electrochromic Windows in the US Commercial Buildings Sector*. Lawrence Berkeley National Laboratory **2004**.
- (9) Lampert, C.M. Electrochromic Materials and Devices for Energy Efficient Windows *Sol. Energy Mater.* **1984**, 11, 1–27.
- (10) Jittiarporn, P.; Badilescu, S.; Al Sawaf, M. N.; Sikong, L.; Truong, V. Van. Electrochromic Properties of Sol–Gel Prepared Hybrid Transition Metal Oxides – A

Short Review. *J. Sci. Adv. Mater. Devices* **2017**, 2, 286–300.

- (11) Song, Y.; Wang, H.; Li, Z.; Ye, N.; Wang, L.; Liu, Y. $H_xMoO_3@C$ Nanobelts: Green Synthesis and Superior Lithium Storage Properties. *Int. J. Hydrogen Energy* **2015**, 40, 3613–3623.
- (12) Ressouche, E.; Kernavanois, N.; Regnault, L. P.; Henry, J. Y. Magnetic Structures of the Metal Monoxides NiO and CoO Re-Investigated by Spherical Neutron Polarimetry. *Phys. B Condens. Matter* **2006**, 385, 394–397.
- (13) Hu, J.; Zhu, K.; Chen, L.; Yang, H.; Li, Z.; Suchopar, A.; Richards, R. Preparation and Surface Activity of Single-Crystalline NiO(111) Nanosheets with Hexagonal Holes: A Semiconductor Nanospanner. *Adv. Mater.* **2008**, 20, 267–271.
- (14) Mortimer, R. J. Organic Electrochromic Materials. *Electrochim. Acta* **1999**, 44, 2971–2981.
- (15) Kaneto, K.; Takeda, S.; Yoshino, K. Characteristics of Heterojunction Consisting of Conducting Polymers of Polythiophene and Polypyrrole. *Jpn. J. Appl. Phys.* **1985**, 24, L553–L555.
- (16) Huang, Y.; Zhu, M.; Huang, Y.; Meng, W.; Gong, Q.; Li, G.; Zhi, C. An Electrochromic Supercapacitor and Its Hybrid Derivatives: Quantifiably Determining Their Electrical Energy Storage by an Optical Measurement. *J. Mater. Chem. A* **2015**, 3, 21321–21327.
- (17) Zhang, J.; Tu, J. P.; Xia, X. H.; Qiao, Y.; Lu, Y. An All-Solid-State Electrochromic Device Based on NiO/ WO_3 complementary Structure and Solid Hybrid Polyelectrolyte. *Sol. Energy Mater. Sol. Cells* **2009**, 93, 1840–1845.
- (18) Liu, X.; Zhang, J. Z.; Huang, K. J.; Hao, P. Net-like Molybdenum Selenide-

- Acetylene Black Supported on Ni Foam for High-Performance Supercapacitor Electrodes and Hydrogen Evolution Reaction. *Chem. Eng. J.* **2016**, *302*, 437-445.
- (19) Liu, C.; Li, F.; Lai-Peng, M.; Cheng, H. M. Advanced Materials for Energy Storage. *Adv. Mater.* **2010**, *22*, E28-E62.
- (20) Xia, X. H.; Tu, J. P.; Mai, Y. J.; Wang, X. L.; Gu, C. D.; Zhao, X. B. Self-Supported Hydrothermal Synthesized Hollow Co_3O_4 Nanowire Arrays with High Supercapacitor Capacitance. *J. Mater. Chem.* **2011**, *21*, 9319-9325.
- (21) Zhang, K.; Zhang, L. L.; Zhao, X. S.; Wu, J. Graphene/Polyaniline Nanofiber Composites as Supercapacitor Electrodes. *Chem. Mater.* **2010**, *22*, 1392-1401.
- (22) Dong, X.; Wang, L.; Wang, D.; Li, C.; Jin, J. Layer-by-Layer Engineered Co-Al Hydroxide Nanosheets/Graphene Multilayer Films as Flexible Electrode for Supercapacitor. *Langmuir* **2012**, *28*, 293-298.
- (23) Santos, L.; Neto, J. P.; Crespo, A.; Baião, P.; Barquinha, P.; Pereira, L.; Martins, R.; Fortunato, E. Electrodeposition of WO_3 Nanoparticles for Sensing Applications. In *Electroplating of Nanostructures*; **2015**, 27-48.
- (24) Chauhan, I.; Mohanty, P. Immobilization of Titania Nanoparticles on the Surface of Cellulose Fibres by a Facile Single Step Hydrothermal Method and Study of Their Photocatalytic and Antibacterial Activities. *RSC Adv.* **2014**, *4*, 57885-57890.
- (25) Li, H.; Chen, J.; Cui, M.; Cai, G.; Eh, A. L. S.; Lee, P. S.; Wang, H.; Zhang, Q.; Li, Y. Spray Coated Ultrathin Films from Aqueous Tungsten Molybdenum Oxide Nanoparticle Ink for High Contrast Electrochromic Applications. *J. Mater. Chem. C* **2015**, *4*, 33-38.
- (26) Costa, C.; Pinheiro, C.; Henriques, I.; Laia, C. A. T. Inkjet Printing of Sol-Gel

- Synthesized Hydrated Tungsten Oxide Nanoparticles for Flexible Electrochromic Devices. *ACS Appl. Mater. Interfaces* **2012**, *4*, 1330-1340.
- (27) Cai, G.; Darmawan, P.; Cheng, X.; Lee, P. S. Inkjet Printed Large Area Multifunctional Smart Windows. *Adv. Energy Mater.* **2017**, *7*, 1602598.
 - (28) Thakur, V. K.; Ding, G.; Ma, J.; Lee, P. S.; Lu, X. Hybrid Materials and Polymer Electrolytes for Electrochromic Device Applications. *Adv. Mater.* **2012**, *24*, 4071-4096.
 - (29) Zhang, W.; Li, H.; Firby, C. J.; Al-hussein, M.; Elezzabi, A. Y. Oxygen-Vacancy-Tunable Electrochemical Properties of Electrodeposited Molybdenum Oxide Films. **2019**, *11*, 20378-20385.
 - (30) Li, H.; McRae, L.; Firby, C. J.; Al-Hussein, M.; Elezzabi, A. Y. Nanohybridization of Molybdenum Oxide with Tungsten Molybdenum Oxide Nanowires for Solution-Processed Fully Reversible Switching of Energy Storing Smart Windows. *Nano Energy* **2018**, *47*, 130–139.
 - (31) Hosseini, S. E.; Wahid, M. A. Hydrogen Production from Renewable and Sustainable Energy Resources: Promising Green Energy Carrier for Clean Development. *Renew. Sustain. Energy Rev.* **2016**, *57*, 850–866.
 - (32) Lee, S.-T.; Sheng, M.; Lifshitz, Y.; Lin, H.; Liao, F.; Zhu, L.; Shao, M.; Li, Y. A Rhodium/Silicon Co-Electrocatalyst Design Concept to Surpass Platinum Hydrogen Evolution Activity at High Overpotentials. *Nat. Commun.* **2016**, *7*, 1–7.
 - (33) Chen, P.; Shen, G.; Shi, Y.; Chen, H.; Zhou, C. Preparation and Characterization of Flexible Asymmetric Supercapacitors. *ACS Nano* **2010**, *4*, 4403–4411.
 - (34) Yuan, C.; Wu, H. Bin; Xie, Y.; Lou, X. W. Mixed Transition-Metal Oxides: Design,

- Synthesis, and Energy-Related Applications. *Angew. Chemie, Int. Ed.* **2014**, *53*, 1488–1504.
- (35) Mendoza-Sánchez, B.; Brousse, T.; Ramirez-Castro, C.; Nicolosi, V.; S. Grant, P. An Investigation of Nanostructured Thin Film α -MoO₃ based Supercapacitor Electrodes in an Aqueous Electrolyte. *Electrochim. Acta* **2013**, *91*, 253–260.
- (36) Hou, S.; Zhang, G.; Zeng, W.; Zhu, J.; Gong, F.; Li, F.; Duan, H. Hierarchical Core-Shell Structure of ZnO Nanorod@NiO/MoO₂ composite Nanosheet Arrays for High-Performance Supercapacitors. *ACS Appl. Mater. Interfaces* **2014**, *6*, 13564–13570.
- (37) Thangasamy, P.; Ilayaraja, N.; Jeyakumar, D.; Sathish, M. Electrochemical Cycling and beyond: Unrevealed Activation of MoO₃ for Electrochemical Hydrogen Evolution Reactions. *Chem. Commun.* **2017**, *53*, 2245–2248.
- (38) Wang, W.; Qin, J.; Yin, Z.; Cao, M. Achieving Fully Reversible Conversion in MoO₃ for Lithium Ion Batteries by Rational Introduction of CoMoO₄. *ACS Nano* **2016**, *10*, 10106–10116.
- (39) Li, H.; Mcrae, L.; Firby, C. J.; Elezzabi, A. Y. Rechargeable Aqueous Electrochromic Batteries Utilizing Ti-Substituted Tungsten Molybdenum Oxide Based Zn²⁺ Ion Intercalation Cathodes. **2019**, *31*, 1807065.
- (40) Li, H.; Li, J.; Hou, C.; Ho, D.; Zhang, Q.; Li, Y.; Wang, H. Solution-Processed Porous Tungsten Molybdenum Oxide Electrodes for Energy Storage Smart Windows. *Adv. Mater. Technol.* **2017**, *2*, 2–7.
- (41) Li, H.; McRae, L.; Elezzabi, A. Y. Solution-Processed Interfacial PEDOT:PSS Assembly into Porous Tungsten Molybdenum Oxide Nanocomposite Films for Electrochromic Applications. *ACS Appl. Mater. Interfaces* **2018**, *10*, 10520-10527.

- (42) Iriyama, Y.; Abe, T.; Inaba, M.; Ogumi, Z. Transmission Electron Microscopy (TEM) Analysis of Two-Phase Reaction in Electrochemical Lithium Insertion within α -MoO₃. *Solid State Ionics* **2000**, *135*, 95–100.
- (43) Tsumura, T.; Inagaki, M. Lithium Insertion/Extraction Reaction on Crystalline MoO₃. *Solid State Ionics* **1997**, *104*, 183–189.
- (44) Kim, H. S.; Cook, J. B.; Lin, H.; Ko, J. S.; Tolbert, S. H.; Ozolins, V.; Dunn, B. Oxygen Vacancies Enhance Pseudocapacitive Charge Storage Properties of MoO_{3-x}. *Nat. Mater.* **2017**, *16*, 454–462.
- (45) Balendhran, S.; Deng, J.; Ou, J. Z.; Walia, S.; Scott, J.; Tang, J.; Wang, K. L.; Field, M. R.; Russo, S.; Zhuiykov, S.; et al. Enhanced Charge Carrier Mobility in Two-Dimensional High Dielectric Molybdenum Oxide. *Adv. Mater.* **2013**, *25*, 109–114.
- (46) Yu, M.; Cheng, X.; Zeng, Y.; Wang, Z.; Tong, Y.; Lu, X.; Yang, S. Dual-Doped Molybdenum Trioxide Nanowires: A Bifunctional Anode for Fiber-Shaped Asymmetric Supercapacitors and Microbial Fuel Cells. *Angew. Chemie, Int. Ed.* **2016**, *55*, 6762–6766.
- (47) Liu, C.; Li, Z.; Zhang, Z. Molybdenum Oxide Film with Stable Pseudocapacitive Property for Aqueous Micro-Scale Electrochemical Capacitor. *Electrochim. Acta* **2014**, *134*, 84–91.
- (48) Choi, H.; Heo, J. H.; Ha, S.; Kwon, B. W.; Yoon, S. P.; Han, J.; Kim, W. S.; Im, S. H.; Kim, J. Facile Scalable Synthesis of MoO₂ nanoparticles by New Solvothermal Cracking Process and Their Application to Hole Transporting Layer for CH₃NH₃PbI₃ planar Perovskite Solar Cells. *Chem. Eng. J.* **2017**, *310*, 179–186.
- (49) de Castro, I. A.; Datta, R. S.; Ou, J. Z.; Castellanos-Gomez, A.; Sriram, S.; Daeneke,

- T.; Kalantar-zadeh, K. Molybdenum Oxides – From Fundamentals to Functionality. *Adv. Mater.* **201**, 29, 1701619.
- (50) Jiang, J.; Li, Y.; Liu, J.; Huang, X.; Yuan, C.; Lou, X. W. Recent Advances in Metal Oxide-Based Electrode Architecture Design for Electrochemical Energy Storage. *Adv. Mater.* **2012**, 24, 5166–5180.
- (51) Dharmadasa, I. M.; Haigh, J. Strengths and Advantages of Electrodeposition as a Semiconductor Growth Technique for Applications in Microelectronic Devices. *J. Electrochem. Soc.* **2006**, 153, G47-G52.
- (52) Ruythooren, W.; Attenborough, K.; Beerten, S.; Merken, P.; Fransaeer, J.; Beyne, E.; Van Hoof, C.; De Boeck, J.; Celis, J. P. Electrodeposition for the Synthesis of Microsystems. *J. Micromechanics Microengineering* **2000**, 10, 101–107.
- (53) Maxfield, M.; Eckhardt, H.; Iqbal, Z.; Reidinger, F.; Baughman, R. H. Bi-Sr-Ca-Cu-O and Pb-Bi-Sr-Ca-Cu-O Superconductor Films via an Electrodeposition Process. *Appl. Phys. Lett.* **1989**, 54, 1932–1933.
- (54) Li, H.; Wang, J.; Shi, Q.; Zhang, M.; Hou, C.; Shi, G.; Wang, H.; Zhang, Q.; Li, Y.; Chi, Q. Constructing Three-Dimensional Quasi-Vertical Nanosheet Architectures from Self-Assemble Two-Dimensional $\text{WO}_3 \cdot 2\text{H}_2\text{O}$ for Efficient Electrochromic Devices. *Appl. Surf. Sci.* **2016**, 380, 281-287.
- (55) Jia, H.; Chen, Z.; Liu, Z.; Zhao, J.; Ding, C.; Yang, H.; Zhang, W.; Liu, X.; Qiu, J. $\text{CaF}_2\text{:Eu}$ Films Shine Novel Blue, White or Red Luminescence Though Adjustment of the Valence State of Eu Ions Using the Electro-Deposition Method. *J. Mater. Chem. C* **2017**, 5, 12085–12089.
- (56) Liu, C.; Long, Y.; Magdassi, S.; Mandler, D. Ionic Strength Induced

- Electrodeposition: A Universal Approach for Nanomaterial Deposition at Selective Areas. *Nanoscale* **2017**, *9*, 485–490.
- (57) Gan, J.; Lu, X.; Wu, J.; Xie, S.; Zhai, T.; Yu, M.; Zhang, Z.; Mao, Y.; Wang, S. C. I.; Shen, Y.; et al. Oxygen Vacancies Promoting Photoelectrochemical Performance of In₂O₃ Nanocubes. *Sci. Rep.* **2013**, *3*, 1–7.
- (58) Zhai, T.; Xie, S.; Yu, M.; Fang, P.; Liang, C.; Lu, X.; Tong, Y. Oxygen Vacancies Enhancing Capacitive Properties of MnO₂ nanorods for Wearable Asymmetric Supercapacitors. *Nano Energy* **2014**, *8*, 255–263.
- (59) Wang, S.-Q.; Cai, X.; Song, Y.; Sun, X.; Liu, X.-X. VO_x@MoO₃ Nanorod Composite for High-Performance Supercapacitors. *Adv. Funct. Mater.* **2018**, *28*, 1803901.
- (60) Rajeswari, J.; Kishore, P. S.; Viswanathan, B.; Varadarajan, T. K. One-Dimensional MoO₂ nanorods for Supercapacitor Applications. *Electrochem. commun.* **2009**, *11*, 572-575.
- (61) Li, X.; Jiang, Y.; Jia, L.; Wang, C. MoO₂ nanoparticles on Reduced Graphene Oxide/Polyimide-Carbon Nanotube Film as Efficient Hydrogen Evolution Electrocatalyst. *J. Power Sources* **2016**, *304*, 146-164.
- (62) Baeck, S. H.; Choi, K. S.; Jaramillo, T. F.; Stucky, G. D.; McFarland, E. W. Enhancement of Photocatalytic and Electrochromic Properties of Electrochemically Fabricated Mesoporous WO₃ Thin Films. *Adv. Mater.* **2003**, *15*, 1269–1273.
- (63) Kim, C. Y.; Cho, S. G.; Park, S.; Choi, D. K. Tungsten Oxide Film Synthesis by Spray Pyrolysis of Peroxotungstic Acid and Its Electrochromic Characterization. *J. Ceram. Process. Res.* **2009**, *10*, 851-854.

- (64) Zhou, E.; Wang, C.; Zhao, Q.; Li, Z.; Shao, M.; Deng, X.; Liu, X.; Xu, X. Facile Synthesis of MoO₂ nanoparticles as High Performance Supercapacitor Electrodes and Photocatalysts. *Ceram. Int.* **2016**, *42*, 2198–2203.
- (65) Li, H.; Chen, J.; Cui, M.; Cai, G.; Eh, A. L. S.; Lee, P. S.; Wang, H.; Zhang, Q.; Li, Y. Spray Coated Ultrathin Films from Aqueous Tungsten Molybdenum Oxide Nanoparticle Ink for High Contrast Electrochromic Applications. *J. Mater. Chem. C* **2015**, *4*, 33–38.
- (66) Liang, L.; Zhang, J.; Zhou, Y.; Xie, J.; Zhang, X.; Guan, M.; Pan, B.; Xie, Y. High-Performance Flexible Electrochromic Device Based on Facile Semiconductor-To-Metal Transition Realized by WO₃·2H₂O Ultrathin Nanosheets. *Sci. Rep.* **2013**, *3*, 1–8.
- (67) Icaza, J. C.; Guduru, R. K. Characterization of α -MoO₃ anode with Aqueous Beryllium Sulfate for Supercapacitors. *J. Alloys Compd.* **2017**, *726*, 453–459.
- (68) Zhuang, Q.-C.; Wei, T.; Du, L.-L.; Cui, Y.-L.; Fang, L.; Sun, S.-G. An Electrochemical Impedance Spectroscopic Study of the Electronic and Ionic Transport Properties of Spinel LiMn₂O₄. *J. Phys. Chem. C* **2010**, *114*, 8614–8621.
- (69) Noh, J.; Yoon, C. M.; Kim, Y. K.; Jang, J. High Performance Asymmetric Supercapacitor Twisted from Carbon Fiber/MnO₂ and Carbon Fiber/MoO₃. *Carbon N. Y.* **2017**, *116*, 470–478.
- (70) Winchester, A.; Ghosh, S.; Feng, S.; Elias, A. L.; Mallouk, T.; Terrones, M.; Talapatra, S. Electrochemical Characterization of Liquid Phase Exfoliated Two-Dimensional Layers of Molybdenum Disulfide. *ACS Appl. Mater. Interfaces* **2014**, *6*, 2125–2130.

- (71) Eric Shen, D.; Österholm, A. M.; Reynolds, J. R. Out of Sight but Not out of Mind: The Role of Counter Electrodes in Polymer-Based Solid-State Electrochromic Devices. *J. Mater. Chem. C* **2015**, *3*, 9715-9725.
- (72) Nwanya, A. C.; Jafta, C. J.; Ejikeme, P. M.; Ugwuoke, P. E.; Reddy, M. V.; Osuji, R. U.; Ozoemena, K. I.; Ezema, F. I. Electrochromic and Electrochemical Capacitive Properties of Tungsten Oxide and Its Polyaniline Nanocomposite Films Obtained by Chemical Bath Deposition Method. *Electrochim. Acta* **2014**, *128*, 218–225.
- (73) Li, L.; Zhang, T.; Yan, J.; Cai, X.; Liu, S. F. P Doped MoO_{3-x} Nanosheets as Efficient and Stable Electrocatalysts for Hydrogen Evolution. *Small* **2017**, *13*, 2–8.
- (74) Chen, Y. Y.; Zhang, Y.; Zhang, X.; Tang, T.; Luo, H.; Niu, S.; Dai, Z. H.; Wan, L. J.; Hu, J. S. Self-Templated Fabrication of MoNi₄/MoO_{3-x} Nanorod Arrays with Dual Active Components for Highly Efficient Hydrogen Evolution. *Adv. Mater.* **2017**, *29*, 1703311.
- (75) Datta, R. S.; Haque, F.; Mohiuddin, M.; Carey, B. J.; Syed, N.; Zavabeti, A.; Zhang, B.; Khan, H.; Berean, K. J.; Ou, J. Z.; et al. Highly Active Two Dimensional α -MoO_{3-x} for the Electrocatalytic Hydrogen Evolution Reaction. *J. Mater. Chem. A* **2017**, *5*, 24223–24231.
- (76) Luo, Z.; Miao, R.; Huan, T. D.; Mosa, I. M.; Poyraz, A. S.; Zhong, W.; Cloud, J. E.; Kriz, D. A.; Thanneeru, S.; He, J.; et al. Mesoporous MoO_{3-x} Material as an Efficient Electrocatalyst for Hydrogen Evolution Reactions. *Adv. Energy Mater.* **2016**, *6*, 1600528.
- (77) Su, C.; Xiang, J.; Wen, F.; Song, L.; Mu, C.; Xu, D.; Hao, C.; Liu, Z. Microwave Synthesized Three-Dimensional Hierarchical Nanostructure CoS₂/MoS₂ Growth on

- Carbon Fiber Cloth: A Bifunctional Electrode for Hydrogen Evolution Reaction and Supercapacitor. *Electrochim. Acta* **2016**, *212*, 941–949.
- (78) Ranaweera, C. K.; Wang, Z.; Alqurashi, E.; Kahol, P. K.; Dvornic, P. R.; Gupta, B. K.; Ramasamy, K.; Mohite, A. D.; Gupta, G.; Gupta, R. K. Highly Stable Hollow Bifunctional Cobalt Sulfides for Flexible Supercapacitors and Hydrogen Evolution. *J. Mater. Chem. A* **2016**, *4*, 9014–9018.
- (79) Li, H.; Wang, J.; Shi, Q.; Zhang, M.; Hou, C.; Shi, G.; Wang, H.; Zhang, Q.; Li, Y.; Chi, Q. Constructing Three-Dimensional Quasi-Vertical Nanosheet Architectures from Self-Assemble Two-Dimensional $\text{WO}_3 \cdot 2\text{H}_2\text{O}$ for Efficient Electrochromic Devices. *Appl. Surf. Sci.* **2016**, *380*, 281–287.
- (80) Alsaif, M. M. Y. A.; Balendhran, S.; Field, M. R.; Latham, K.; Wlodarski, W.; Ou, J. Z.; Kalantar-Zadeh, K. Two Dimensional $\alpha\text{-MoO}_3$ nanoflakes Obtained Using Solvent-Assisted Grinding and Sonication Method: Application for H_2 gas Sensing. *Sensors Actuators, B Chem.* **2014**, *192*, 196–204.
- (81) Cai, G.; Wang, J.; Lee, P. S. Next-Generation Multifunctional Electrochromic Devices. *Acc. Chem. Res.* **2016**, *49*, 1469–1476.
- (82) Zhang, W.; Wang, X.; Wang, Y.; Yang, G.; Gu, C.; Zheng, W.; Zhang, Y. M.; Li, M.; Zhang, S. X. A Bio-Inspired Ultra-High Energy Efficiency Bistable Electronic Billboard and Reader. *Nat. Commun.* **2019**, *10*, 1559.
- (83) Cho, S. Il; Kwon, W. J.; Choi, S. J.; Kim, P.; Park, S. A.; Kim, J.; Son, S. J.; Xiao, R.; Kim, S. H.; Lee, S. B. Nanotube-Based Ultrafast Electrochromic Display. *Adv. Mater.* **2005**, *17*, 171–175.
- (84) Sun, X. W.; Wang, J. X. Fast Switching Electrochromic Display Using a Viologen-

- Modified ZnO Nanowire Array Electrode. *Nano Lett.* **2008**, *8*, 1884-1889.
- (85) Li, G.; Zhang, B.; Wang, J.; Zhao, H.; Ma, W.; Xu, L.; Zhang, W.; Zhou, K.; Du, Y.; He, G. Electrochromic Poly(Chalcogenoviologen)s as Anode Materials for High-Performance Organic Radical Lithium-Ion Batteries. *Angew. Chemie, Int. Ed.* **2019**, *58*, 8468-8473.
- (86) Li, X.; Du, Z.; Song, Z.; Li, B.; Wu, L.; Liu, Q.; Zhang, H.; Li, W. Bringing Hetero-Polyacid-Based Underwater Adhesive as Printable Cathode Coating for Self-Powered Electrochromic Aqueous Batteries. *Adv. Funct. Mater.* **2018**, *28*, 1800599.
- (87) Zhang, S.; Cao, S.; Zhang, T.; Fisher, A.; Lee, J. Y. Al^{3+} Intercalation/de-Intercalation-Enabled Dual-Band Electrochromic Smart Windows with a High Optical Modulation, Quick Response and Long Cycle Life. *Energy Environ. Sci.* **2018**, *11*, 2884–2892.
- (88) Zhang, S.; Cao, S.; Zhang, T.; Yao, Q.; Fisher, A.; Lee, J. Y. Monoclinic Oxygen-Deficient Tungsten Oxide Nanowires for Dynamic and Independent Control of near-Infrared and Visible Light Transmittance. *Mater. Horizons* **2018**, *5*, 291–297.
- (89) Cao, S.; Zhang, S.; Zhang, T.; Yao, Q.; Lee, J. Y. A Visible Light-Near-Infrared Dual-Band Smart Window with Internal Energy Storage. *Joule* **2019**, *3*, 1152-1162.
- (90) Scherer, M. R. J.; Li, L.; Cunha, P. M. S.; Scherman, O. A.; Steiner, U. Enhanced Electrochromism in Gyroid-Structured Vanadium Pentoxide. *Adv. Mater.* **2012**, *24*, 1217-1221.
- (91) Wei, D.; Scherer, M. R. J.; Bower, C.; Andrew, P.; Ryhänen, T.; Steiner, U. A Nanostructured Electrochromic Supercapacitor. *Nano Lett.* **2012**, *12*, 1857-1862.
- (92) Tong, Z.; Li, N.; Lv, H.; Tian, Y.; Qu, H.; Zhang, X.; Zhao, J.; Li, Y. Annealing

- Synthesis of Coralline V₂O₅ Nanorod Architecture for Multicolor Energy-Efficient Electrochromic Device. *Sol. Energy Mater. Sol. Cells* **2016**, *146*, 135-143.
- (93) Zhang, K.; Li, N.; Ma, X.; Wang, Y.; Zhao, J.; Qiang, L.; Li, X.; Li, Y. Building Ultrathin Polyaniline Encapsulated V₂O₅ Heterogeneous Nanowires and Its Electrochromic Performance. *J. Electroanal. Chem.* **2018**, *825*, 16-21.
- (94) Karaca, G. Y.; Eren, E.; Alver, C.; Koc, U.; Uygun, E.; Oksuz, L.; Oksuz, A. U. Plasma Modified V₂O₅/PEDOT Hybrid Based Flexible Electrochromic Devices. *Electroanalysis* **2017**, *29*, 1323-1331.
- (95) Gu, S.; Wang, H.; Wu, C.; Bai, Y.; Li, H.; Wu, F. Confirming Reversible Al³⁺ Storage Mechanism through Intercalation of Al³⁺ into V₂O₅ Nanowires in a Rechargeable Aluminum Battery. *Energy Storage Mater.* **2017**, *6*, 9-17.
- (96) Li, H.; Li, J.; Hou, C.; Ho, D.; Zhang, Q.; Li, Y.; Wang, H. Solution-Processed Porous Tungsten Molybdenum Oxide Electrodes for Energy Storage Smart Windows. *Adv. Mater. Technol.* **2017**, *2*, 1700047.
- (97) Paik, T.; Hong, S. H.; Gaulding, E. A.; Caglayan, H.; Gordon, T. R.; Engheta, N.; Kagan, C. R.; Murray, C. B. Solution-Processed Phase-Change VO₂ Metamaterials from Colloidal Vanadium Oxide (VO_x) Nanocrystals. *ACS Nano* **2014**, *8*, 797–806.
- (98) Ming, F.; Liang, H.; Lei, Y.; Kandambeth, S.; Eddaoudi, M.; Alshareef, H. N. Layered Mg_xV₂O₅·nH₂O as Cathode Material for High-Performance Aqueous Zinc Ion Batteries. *ACS Energy Lett.* **2018**, *3*, 2602-2609.
- (99) Yan, M.; He, P.; Chen, Y.; Wang, S.; Wei, Q.; Zhao, K.; Xu, X.; An, Q.; Shuang, Y.; Shao, Y.; et al. Water-Lubricated Intercalation in V₂O₅·nH₂O for High-Capacity and High-Rate Aqueous Rechargeable Zinc Batteries. *Adv. Mater.* **2018**, *30*, 1703725.

- (100) Yue, Y.; Li, H.; Li, K.; Wang, J.; Wang, H.; Zhang, Q.; Li, Y.; Chen, P. High-Performance Complementary Electrochromic Device Based on $\text{WO}_3 \cdot 0.33\text{H}_2\text{O}$ /PEDOT and Prussian Blue Electrodes. *J. Phys. Chem. Solids* **2017**, *110*, 284-289.
- (101) Xiong, C.; Aliev, A. E.; Gnade, B.; Balkus, K. J. Fabrication of Silver Vanadium Oxide and V_2O_5 Nanowires for Electrochromics. *ACS Nano* **2008**, *2*, 293-301.
- (102) Kang, W.; Yan, C.; Wang, X.; Foo, C. Y.; Ming Tan, A. W.; Zhi Chee, K. J.; Lee, P. S. Green Synthesis of Nanobelt-Membrane Hybrid Structured Vanadium Oxide with High Electrochromic Contrast. *J. Mater. Chem. C* **2014**, *2*, 4827-4732.
- (103) Wang, R. Y.; Shyam, B.; Stone, K. H.; Weker, J. N.; Pasta, M.; Lee, H. W.; Toney, M. F.; Cui, Y. Reversible Multivalent (Monovalent, Divalent, Trivalent) Ion Insertion in Open Framework Materials. *Adv. Energy Mater.* **2015**, *5*, 1401869.
- (104) He, P.; Quan, Y.; Xu, X.; Yan, M.; Yang, W.; An, Q.; He, L.; Mai, L. High-Performance Aqueous Zinc-Ion Battery Based on Layered $\text{H}_2\text{V}_3\text{O}_8$ Nanowire Cathode. *Small* **2017**, *13*, 1702551.
- (105) Wen, R. T.; Granqvist, C. G.; Niklasson, G. A. Eliminating Degradation and Uncovering Ion-Trapping Dynamics in Electrochromic WO_3 Thin Films. *Nat. Mater.* **2015**, *14*, 996-1001.
- (106) Silversmit, G.; Depla, D.; Poelman, H.; Marin, G. B.; De Gryse, R. Determination of the V2p XPS Binding Energies for Different Vanadium Oxidation States (V^{5+} to V^{0+}). *J. Electron Spectros. Relat. Phenomena* **2004**, *135*, 167-175.
- (107) Liu, P.; Bian, K.; Zhu, K.; Xu, Y.; Gao, Y.; Luo, H.; Lu, L.; Wang, J.; Liu, J.; Tai, G. Ultrathin Nanoribbons of in Situ Carbon-Coated $\text{V}_3\text{O}_7 \cdot \text{H}_2\text{O}$ for High-Energy and

- Long-Life Li-Ion Batteries: Synthesis, Electrochemical Performance, and Charge-Discharge Behavior. *ACS Appl. Mater. Interfaces* **2017**, *9*, 17002-17012.
- (108) Wang, J.; Zhang, L.; Yu, L.; Jiao, Z.; Xie, H.; Lou, X. W.; Wei Sun, X. A Bi-Functional Device for Self-Powered Electrochromic Window and Self-Rechargeable Transparent Battery Applications. *Nat. Commun.* **2014**, *5*, 4921.
- (109) Cheng, W.; He, J.; Dettelbach, K. E.; Johnson, N. J. J.; Sherbo, R. S.; Berlinguette, C. P. Photodeposited Amorphous Oxide Films for Electrochromic Windows. *Chem* **2018**, *4*, 821-832.
- (110) Wang, M.; Xing, X.; Perepichka, I. F.; Shi, Y.; Zhou, D.; Wu, P.; Meng, H. Electrochromic Smart Windows Can Achieve an Absolute Private State through Thermochromically Engineered Electrolyte. *Adv. Energy Mater.* **2019**, *9*, 1900433.
- (111) Azam, A.; Kim, J.; Park, J.; Novak, T. G.; Tiwari, A. P.; Song, S. H.; Kim, B.; Jeon, S. Two-Dimensional WO₃ Nanosheets Chemically Converted from Layered WS₂ for High-Performance Electrochromic Devices. *Nano Lett.* **2018**, 5646-5651.
- (112) Zhang, S.; Cao, S.; Zhang, T.; Yao, Q.; Lin, H.; Fisher, A.; Lee, J. Y. Overcoming the Technical Challenges in Al Anode-Based Electrochromic Energy Storage Windows. *Small Methods* **2019**, *4*, 1900545.
- (113) Zhang, S.; Li, Y.; Zhang, T.; Cao, S.; Yao, Q.; Lin, H.; Ye, H.; Fisher, A.; Lee, J. Y. Dual-Band Electrochromic Devices with a Transparent Conductive Capacitive Charge-Balancing Anode. *ACS Appl. Mater. Interfaces* **2019**, *11*, 48062-48070.
- (114) Lang, A. W.; Li, Y.; De Keersmaecker, M.; Shen, D. E.; Österholm, A. M.; Berglund, L.; Reynolds, J. R. Transparent Wood Smart Windows: Polymer Electrochromic Devices Based on Poly(3,4-Ethylenedioxythiophene):Poly(Styrene Sulfonate)

Electrodes. *ChemSusChem* **2018**, 11, 854-863.